Article

Formation of Transitional cE/UCD Galaxies through Massive/Dwarf Disc Galaxy Mergers

Alexander V. Khoperskov *,† , **Sergey S. Khrapov** † and **Danila S. Sirotin** †

Department of Information Systems and Computer Modelling, Volgograd State University, Universitetsky pr., 100, Volgograd 400062, Russia; khrapov@volsu.ru (S.S.K.); d.sirotin@volsu.ru (D.S.S.)
* Correspondence: khoperskov@volsu.ru
† These authors contributed equally to this work.

Abstract: The dynamics of the merger of a dwarf disc galaxy with a massive spiral galaxy of the Milky Way type were studied in detail. The remnant of such interaction after numerous crossings of the satellite through the disc of the main galaxy was a compact stellar core, the characteristics of which were close to small compact elliptical galaxies (cEs) or large ultra-compact dwarfs (UCDs). Such transitional cE/UCD objects with an effective radius of 100–200 pc arise as a result of stripping the outer layers of the stellar core during the destruction of a dwarf disc galaxy. Numerical models of the satellite before interaction included baryonic matter (stars and gas) and dark mass. We used N-body to describe the dynamics of stars and dark matter, and we used smoothed-particle hydrodynamics to model the gas components of both galaxies. The direct method of calculating the gravitational force between all particles provided a qualitative resolution of spatial structures up to 10 pc. The dwarf galaxy fell onto the gas and stellar discs of the main galaxy almost along a radial trajectory with a large eccentricity. This ensured that the dwarf crossed the disc of the main galaxy at each pericentric approach over a time interval of more than 9 billion years. We varied the gas mass and the initial orbital characteristics of the satellite over a wide range, studying the features of mass loss in the core. The presence of the initial gas component in a dwarf galaxy significantly affects the nature of the formation and evolution of the compact stellar core. The gas-rich satellite gives birth to a more compact elliptical galaxy compared to the merging gas-free dwarf galaxy. The initial gas content in the satellite also affects the internal rotation in the stripped nucleus. The simulated cE/UCD galaxies contained very little gas and dark matter at the end of their evolution.

Keywords: minor merger; Milky-Way-like galaxy; compact elliptical galaxies; ultra-compact dwarf galaxies; N-body simulation; computational fluid dynamics

1. Introduction

The properties of dwarf galaxies vary over extremely wide ranges of sizes and masses, occupying the entire interval from globular clusters (GCs) to objects with a mass of several billion solar masses and a characteristic radius of several kiloparsecs. The entire zoo of dwarfs is numerous and diverse, being, on the one hand, the building material in the hierarchical clustering scenario [1–10] while, on the other hand, they themselves are the result of complex evolution, including the mergers and destruction of different objects [11–14].

Galaxy M32 is the prototype for a class of compact elliptical galaxies (cEs) that are quite rare [5,13,15–18]. Their formation mechanism is usually attributed to tidal influence, as cEs were initially discovered close to giant galaxies in clusters or groups. The typical luminosity of these objects is $\sim 10^9 \, L_\odot$, which is comparable to the luminosity of dwarf elliptical galaxies (dEs). However, the small effective radius $r^{(eff)} \sim 200$–700 pc (see, for example, the sample in the work [13]) gives a high surface brightness, which distinguishes these objects from dwarf elliptical galaxies (dEs). The usual localization of cE galaxies is near central cD-type galaxies. Examples of compact elliptical galaxies near large spiral

galaxies are rarer. Let us point out the SBc-type galaxy PGC057129 (see [19]), the selection of compact objects near disc galaxies in the work [20], in addition to M32 in M31 [11].

Ultra-compact dwarf galaxies (UCDs) were discovered at the turn of the 20th and 21st centuries [21–25]. Subsequent studies have identified UCDs as intermediate in size and brightness between large globular clusters and small dwarf galaxies, with characteristic radii of 10–200 pc and masses of 2×10^6–$5 \times 10^8 \, M_\odot$ [26–32]. Moreover, they differ structurally and dynamically both from GCs and from other types of dwarf galaxies [26,33]. The luminosities of UCDs are between typical values for small dwarf galaxies and large globular clusters. These objects are brighter than GCs; however, it has been proposed that they may be the extremely bright tail of the globular cluster system's distribution. There is a fairly smooth transition of integral characteristics from the brightest globular clusters to UCDs in the presence of important distinctive morphological properties [25].

The locations of UCDs are often grouped closer to the center of rich clusters (e.g., the Fornax, Virgo, and Coma clusters of galaxies) than dwarf galaxies [23], which partly indicates their formation mechanism. The small sizes of cEs and UCDs significantly limits the ability to spatially resolve their internal structure, to estimate the effective radius (half-light radius) and mass through the observed stellar velocities dispersion. Therefore, the required resolution is provided only for nearby galaxies [2–4,34]. An interesting case is the late stage of merging in the disc galaxy NGC 7727 (SABa), where a core with UCD characteristics stands out at a distance of only 480 pc in projection from the center of NGC 7727 with a dynamic mass of $4.2 \times 10^8 \, M_\odot$ [35]. The orbit of this UCD appears to be highly eccentric.

Various scenarios for the formation of ultra-compact dwarf elliptical galaxies have been discussed [13,19,26,27,36,37]. We briefly list them below:

— Reducing the mass of dwarf elliptical galaxies due to tidal influences may be an important mechanism of the galaxy threshing system [13,19]. The outer layers of a stellar system can be effectively removed due to tidal forces in such large clusters as the Fornax Cluster, the Coma Cluster, the Perseus Cluster, and the Virgo Cluster. The threshing rate is higher for highly eccentric orbits compared to the circular motion of the satellite [19]. The compact dwarf core as the basis of UCDs is preserved under strong tidal influences over cosmological times. This mechanism may be sensitive to the initial dark-halo profile of the dwarf galaxy [19]. UCDs can be born from the core of tidally stripped dwarf elliptical galaxies (dEs) or dE/Ns galaxies with low surface brightness [19,36].

— Conditions for UCD formation may be suitable in tidal superclusters that arise from major mergers of galaxies, according to the "Merging Star Cluster Scenario" [27,33,38,39].

— The authors of the work [40] considered the possibility of forming UCDs from supergiant molecular clouds with masses 10^7–$10^8 \, M_\odot$. Hydrodynamic simulations produced clusters with parameters that were typical of ultracompact dwarfs.

— As the sizes of small UCDs and large GCs can be comparable within a sequence with a smooth, continuous distribution of parameters, some common mechanisms for the construction of these objects are discussed, which are the extreme high-luminosity end of the mass function or the result of several associations of large globular clusters [25,41].

— The tidal stripping of a barred disc galaxy in a cluster cD galaxy can form a compact remnant [13]. This conclusion is confirmed by N-body simulations of the evolution of a large S-galaxy such as the Milky Way, which moves in a gravitational potential with parameters similar to those of the Virgo cluster.

— UCDs' radial density profiles satisfy the King model or de Vaucouleurs' law ($\propto \exp(-(r/r^{(eff)})^{1/4})$) [26]. Such ultra-compact objects do not have a massive dark component. This property brings UCDs closer to globular clusters [33].

Types cE and UCD appear to form a continuous sequence of galaxies, which allows us to consider transitional cE/UCD objects [16,29,42]. The observed dependence of stellar velocity dispersion as a function of *B*-band absolute magnitudes shows an example of a smooth transition from cE to UCD [13]. The sizes of some recently dis-

covered UCDs are close to 100–200 pc , which is close to the sizes of small cE galaxies. Examples are NGC936_UCD as a collapsing satellite of the large disc galaxy NGC 936 with $r^{(eff)}$ = 66.5 ± 17 pc [31], the object VUCD7 in the Virgo Cluster with $r^{(eff)} = 96.8$ pc, $M_* = 8.8 \times 10^7 M_\odot$ [18], the galaxy NGC0703-AIMSS1 with $r^{(eff)} = 165$ pc, $M_* = 3.1 \times 10^8 M_\odot$ [20], etc.

The properties of massive GCs, UCDs, and cEs practically fill the entire range of sizes from 5 pc to 600 pc and masses from $2 \times 10^6 M_\odot$ to $6 \times 10^9 M_\odot$ [13,20,29,42]. The overall sample of massive globular clusters, UCDs, and cEs shows a correlation between $r^{(eff)}$ and M_*, although these objects lie in a fairly wide area on the plane $(r^{(eff)}, M_*)$ [29]. At the same time, objects within the types UCD and cE are divided into two groups according to the mechanism of their formation from different mother galaxies [20].

The formation mechanism of the recently discovered isolated compact elliptical galaxies may also be based on tidal stripping, after which, they were thrown out of groups or clusters, due to the dynamic features of the three-body system [17,43]. The authors in [12] relied on combining observational data and IllustrisTNG simulations to analyze the formation of cEs. They concluded that 32 percent in the sample were formed by the merging of a spiral galaxy near a large galaxy and that 68 percent were associated with slow build-up of stellar mass without tidal influence.

High-resolution spectroscopy allows us to determine the internal kinematics of UCDs and CEs [44,45]. Interestingly, the cEs sampled in the work [44] consisted of six rotating compact objects, whose ratio of rotation velocity to velocity dispersion was 0.2–0.5. An important achievement was the discovery that a black hole with a mass of more than $10^6 M_\odot$ in the center of an ultra-compact dwarf galaxy affects the structure and kinematics of the stellar component [46–50]. The presence of supermassive black holes leads to an overestimation of the mass of the stellar population in compact objects [51]. The authors of [45,51] indicated the high prevalence of such systems. Perhaps half of the stripped nuclei contained supermassive black holes [52], the formation of which occurred in the original host galaxy.

Minor merging in a system with a large disc galaxy is accompanied by the tidal stripping of the dwarf and by various disturbances in the main galaxy, including the generation of streams, tails, bridges, and rings [53–57]. Stellar and gas streams are an important source of information about the history of galactic evolution and provide verification of various assumptions, including estimates of dark-mass parameters [58,59]. Close passages of dwarf objects can significantly influence the kinematics and morphology of the disc components of the main galaxy [60–64]. There are numerous examples of observed minor mergers in S-galaxies at different cosmological times. Observations have highlighted cEs/UCDs near large disc galaxies—for example, NGC936_UCD [31], NGC 0703-AIMSS1, NGC 0839-AIMSS1, NGC 1316-AIMSS1, NGC 2768-AIMSS1, NGC 3115-AIMSS1, NGC 4350-AIMSS1, NGC 4546-AIMSS1, NGC4594-UCD1 [20], NGC 0034-S&S1 [65], and NGC 7252-W3 [66]. Moreover, the object NGC936_UCD was the compact core of the destroyed dwarf galaxy MATLAS-167 with a stellar tidal flow. There is reasonable evidence of the passage of the M32 through the center of the M31 disc, which may be the cause of some of the observed features in M31 [61].

Interest in such mergers is fueled by data from the SDSS [67], Gaia [68,69], SEGUE [70], and APOGEE [71,72], the processing of which indicates a possible fall of the satellite Gaia-Sausage-Enceladus (GSE) into our Milky Way about 10 billion years ago [73–77]. The result of this merger was a significant part of the stellar halo, which has complex spatial and kinematic properties [78–81]. Analysis of the structure of phase space and chemical abundance allows us to identify the history of the different substructure formations due to accretion events. Cosmological simulations and N-body merger simulations allow us to trace the process of changes in these phase features [81–87]. The agreement of N-body modeling results with observational data is the basis for determining the parameters of ancient mergers [88]. There are various estimates of the GSE stellar mass before the start of merging within $(0.15–7) \times 10^9 M_\odot$ [73,77,78,89–92].

Our efforts in this work were aimed at studying the possibility of the formation of stellar systems with parameters at the junction of small compact elliptical galaxies and large ultra-compact dwarfs (transitional cEs/UCDs), as a result of the stripping of dwarf galaxies in the field of a Milky-Way-type disc galaxy. We studied the trajectories of the satellite in the most rigid scenario, when it passed through the disc of the main galaxy at each pericentric approach, which corresponded to the initial orbital eccentricity close to unity. Identifying the role of the initial content of the gas component in the satellite on the formation of transitional cEs/UCDs was an important part of our research.

2. Minor-Merger Model

Minor merger means that the mass ratio of two interacting galaxies satisfies the approximate condition $M^{(Sat)}/M^{(MW)} \leq 1/6$, where $M^{(MW)}$ is the mass of a large Milky-Way-type galaxy, and $M^{(Sat)}$ is the satellite mass inside—for example, optical radius R_{opt}. The value of R_{opt} is defined in the model as the radius of a sphere containing approximately 95 percent of the mass of the exponential stellar disc with surface density $\sigma(r) = \sigma_0 \cdot \exp(-r/r_d)$ (r_d is the radial scale of the stellar disc). This profile corresponds approximately to $R_{opt} = 4r_d$. A key property of a minor merger is the ability to preserve the disc of the main galaxy after the merger is completed.

We used mathematical and corresponding numerical models of the dynamics of multi-component galaxies, which are described in the works [93–96]. Gas movement was based on hydrodynamic equations:

$$\frac{\partial \varrho}{\partial t} + \vec{\nabla}(\varrho \vec{u}) = 0, \tag{1}$$

$$\frac{\partial(\varrho \vec{u})}{\partial t} + \vec{\nabla}(\varrho \vec{u} \otimes \vec{u}) = -\vec{\nabla}p - \varrho \vec{\nabla}\Psi, \tag{2}$$

$$\frac{\partial}{\partial t}\left\{\varrho\left(\frac{1}{2}\vec{u}^2 + \varepsilon\right)\right\} + \vec{\nabla}\left\{\varrho\vec{u}\left(\frac{1}{2}\vec{u}^2 + \varepsilon + \Psi\right)\right\} = \varrho Q, \tag{3}$$

where ϱ is the volume gas density, $\vec{u}$ is the velocity vector, p is the pressure, ε is the internal energy, Ψ is the total gravitational potential from gas, stars, and dark matter, and Q is the power of the gas heating and cooling by radiation. The equation of state of an ideal gas with the adiabatic exponent $\gamma = 5/3$ closes the system of Equations (1)–(3).

We used the SPH method to numerically integrate the Equations (1)–(3) [93–96], which has some advantages for modeling interacting multi-component galaxies. Firstly, it is possible to model both the collisional component (gas) and collisionless subsystems (stars and dark matter) in the same way, which is convenient when calculating the gravitational force. Secondly, there is no need for regularization and setting boundary conditions, in contrast to grid methods of computational fluid dynamics. Finally, we can easily track the initial origin of gas during the collision of several galaxies, when strong mixing of gas components occurs [94].

Stars and dark matter were considered as collisionless subsystems and were described by the traditional N-body model:

$$\frac{d\vec{v}_i}{dt} = \vec{f}_i \quad (i = 1, \dots, N), \tag{4}$$

where $\vec{v}_i = \dfrac{d\vec{r}_i}{dt}$ is the velocity of the i-th particle, $\vec{r}_i$ is its radius vector, and $\vec{f}_i$ is the gravitational force acting on the i-th particle from the rest of the mass. The interaction between the gas, the stellar component, and the dark mass of the satellite was carried out by the method of direct summation of forces between all particles,

$$\vec{f}_i = -\sum_{j=1}^{N} G \frac{m_j}{\left(|\vec{r}_{ij}|^2 + \epsilon_c^2\right)^{3/2}} \vec{r}_{ij}, \tag{5}$$

where $j \neq i$, m_j is the mass of *j*-th particle, G is the gravitational constant, $\vec{\mathbf{r}}_{ij} = \vec{\mathbf{r}}_i - \vec{\mathbf{r}}_j$, ϵ_c is the softening length (cutoff radius of the gravitational potential), which ensures collisionlessness for very close passages of two particles, and N is the total number of particles in the model, consisting of gas SPH particles ($N^{(gas)}$), star particles ($N^{(star)}$), and dark-matter particles ($N^{(DM)}$), $N = N^{(gas)} + N^{(star)} + N^{(DM)}$. The basic value of the cutoff radius of the gravitational potential in our models was $\epsilon_c = 10$ pc. The direct method of calculating the gravitational interaction of each particle with each ("Particle–Particle") is very resource-intensive, but gives the best accuracy in modeling a gravitating system, all other things being equal. The use of computing clusters with GPUs for the "Particle–Particle" algorithm provides good resolution with the number of particles 2^{20}–2^{23} [97].

The value of Q for each gas *i*-th particle in the SPH approach in (3) is determined by

$$Q_i = Q_i^{(ex)} + (1 - \alpha_i)Q_i^+ - \alpha_i Q_i^- \, , \tag{6}$$

where $Q_i^{(ex)}$ is the heating of gas particles by external radiation (cosmic rays, stellar radiation), α_i is the coefficient within $0 \leq \alpha_i \leq 1$, $Q_i^- = \varrho_i \Lambda(T_i)$ is the cooling function of SPH particles due to radiation, $Q_i^+ = \sum\limits_{j=1(j \neq i)}^{N^{(gas)}} m_j \alpha_j \Lambda(T_j) W(|\vec{\mathbf{r}}_{ij}|, h_{ij})$ is the heating of the *i*-th particle by radiation from neighboring particles, $\Lambda(T_i)$ is the cooling efficiency, depending on the temperature and gas cooling mechanisms [98,99], W is the SPH kernel [100], and $h_{ij} = \dfrac{h_i + h_j}{2}$, $h_i = \dfrac{4}{3}\left(\dfrac{m_i}{\varrho_i}\right)^{1/3}$ is the smoothing length of the *i*-th particle. We did not consider the detailed processes of chemical dynamics [101,102], limiting ourselves to the energy-balance Equation (3).

The two interacting galaxies differed in their mass by a factor of about 20 within their double optical radii ($2R^{(opt)}$). The first main galaxy corresponded to the characteristics of the Milky Way [93] and will, henceforth, be called the "MW model". We attempted to consider special scenarios for a minor merger to an MW-type galaxy by tracing the evolution of the stripping of a gas-rich dwarf galaxy over more than 9 billion years. Such a model could include a scenario of an event approximately 10 billion years ago associated with the hypothetical object Gaia-Sausage-Enceladus [73,74,77,79,103–107]. The parameters of such minor merging seem to be quite typical both in the past and at low redshifts for a wide range of MW-type galaxies. The initial physical characteristics of the GSE have not yet been precisely determined, despite significant efforts [78,83,88–92,108]. Our satellite model consisted of a rotating star-gas disc inside its dark-matter halo and was located at a distance of $r_0^{(Sat)} > 100$ kpc from the center of the main galaxy at the initial time.

The initial mass-density profiles in the satellite determine the characteristics of the cEs/UCDs. The key role is played by the presence or absence of a nuclear star cluster (NSC) in the satellite [109,110] or a compact pseudo-bulge. The increased density at the center of the stellar component indicates strong deviations from the exponential profile. We considered various mass density distributions in the satellite, including both near-exponential discs without NSC and/or pseudo-bulge and those containing massive nuclear structures with a large concentration of stars.

Figure 1 shows the kinematic characteristics of the main galaxy and the base gas-rich satellite model "G21". The circular velocities $V_c(r)$ of each galaxy are depicted by thick lines. The result of the decomposition of the galaxy models gives the contributions of the various components to V_c. We used the MW model from [93] (Table 1). These parameters were fixed in all the numerical models. The surface density of the MW stellar disc with exponential scale $r_d^{(MW)} = 2.25$ kpc gave an optical radius of approximately $R_{opt}^{(MW)} \simeq 4r_d^{(MW)} = 9$ kpc, which contained more than 90 percent of the stellar disc mass. The stellar component of the satellite was located before the collision inside $R_{opt}^{(Sat)} \simeq 3$ kpc. Figure 1b contains decomposition of the satellite's circular velocity in the model "G21" before its first passage

through the host galaxy at time $t = 0.4$ billion years after the start of the simulation. The total circular velocity of the satellite was also added to Figure 1a, for comparison.
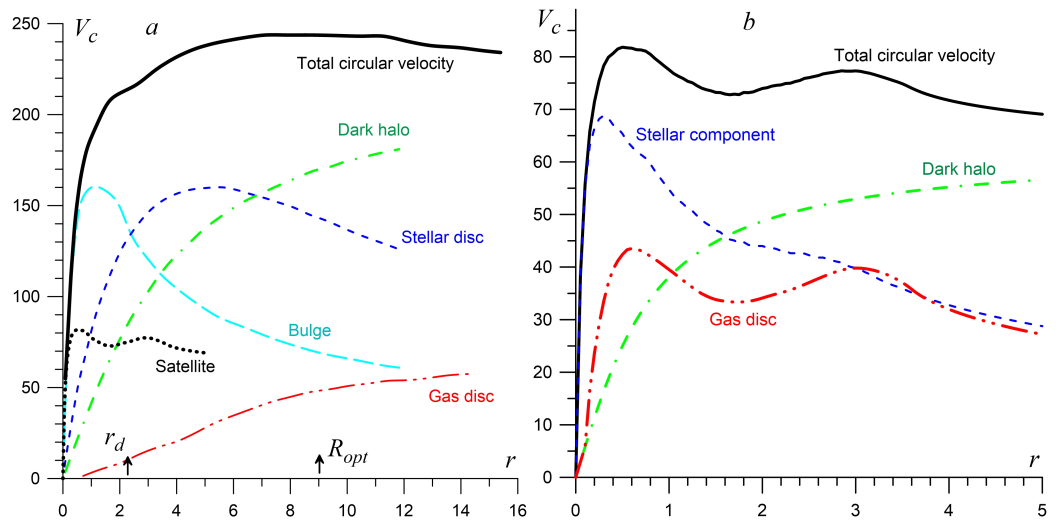
Figure 1. Circular rotation velocities of the MW (**a**) and satellite (**b**) models and the corresponding decompositions into galactic components, $[r] = \text{kpc}$, $[V_c] = \text{km s}^{-1}$.

The initial axisymmetric state of the satellite and MW was constructed based on equilibrium in the radial and vertical directions. The development of non-axisymmetric gravitational instability in the disc was allowed at a subcritical level. As the dark halo did not dominate the central region, the stellar bar was formed before the first passage through the host galaxy. We consider only the centrally symmetric dark halo of the MW, since a triaxial massive halo is capable of generating powerful spiral patterns both in the gas component and the stellar disc, which can redistribute mass along the radius [111,112]. The high gas content ($M_g^{(Sat)} \simeq M_s^{(Sat)}$) in some of our models promoted rapid formation of the bar and spiral pattern. The process of the satellite's fall was accompanied by the increasing influence of tidal forces, which also redistributed the matter in the satellite along the radius. Figure 2 shows the radial surface density profiles of the stellar component in the companion for some models at time $t > 0.4$ billion years before the first crossing of the MW. There are examples both with and without massive concentrated nuclei. All such models contain a stellar bar and a developed spiral structure.
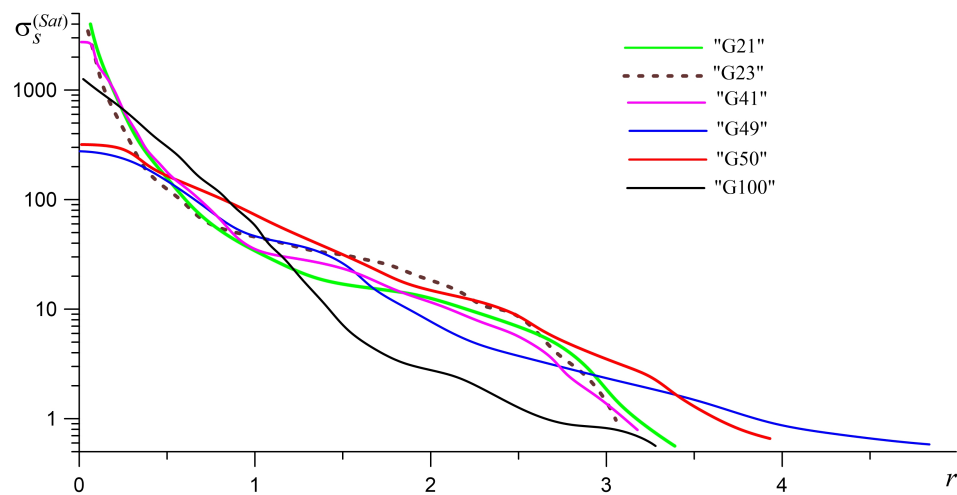
Figure 2. Examples of distributions of azimuthally averaged surface density of stars in different satellite models before the first impact ($[r] = kpc$, $[\sigma_s^{(Sat)}] = M_\odot / pc^2$).

The gas discs were more extensive, extending up to $2R_{opt}^{(MW)}$ in the case of the MW model. The satellite's circular velocity was determined primarily by the stellar component within 1.8 kpc (Figure 1b). The dark halo dominated only at the periphery of the disc, as we were limited to dark-matter profile with a scale of 0.62 kpc without a cusp, in contrast to the NFW model [113]. The maximum gas-rotation velocity in the satellite was about 80 km s^{-1}, which is typical for dwarf S-galaxies [114]. The models of the satellite had different gas contents, from complete absence to mass $M_g^{(Sat)} = M_s^{(Sat)}$. Such gas-rich discs have circular velocities $V_{cg}^{(Sat)} \simeq V_{cs}^{(Sat)}$ at the periphery of the galaxy, where, however, the halo contribution is dominant (Figure 1b). The mass of the Milky Way's dark halo was $M_h^{(MW)}$ inside the optical radius (see Table 1). The parameters of dark matter in both galaxies were constant in all the numerical models. The radial volume density profile in the dark halo corresponded to the quasi-isothermal law $\varrho_h(r) = \varrho_{h0}/(1 + r^2/a^2)$, with $a = 0.62$ kpc in the satellite and $a = 3$ kpc in the MW.

Table 1. Main parameters of the model at the initial time.

Parameter	
Milky-Way model:	
Stellar mass in MW, $M_s^{(MW)}$	$3.72 \times 10^{10} \, M_\odot$
Gas mass, $M_g^{(MW)}$	$0.74 \times 10^{10} \, M_\odot$
Dark-halo mass, $M_{DM}^{(MW)}(r \leq 9\,\text{kpc} = 4r_d^{(MW)})$	$6.02 \times 10^{10} \, M_\odot$
Bulge mass, $M_b^{(MW)}$	$1.0 \times 10^{10} M_\odot$
Bulge scale, $b^{(MW)}$	0.39 kpc
Radial scale of stellar disc, $r_d^{(MW)}$	2.25 kpc
Satellite model:	
Mass of stars in the satellite, $M_s^{(Sat)}$	$0.093 \times 10^{10} \, M_\odot$
Outer boundary of the stellar disc, $R_{opt}^{(Sat)}$	2.7 kpc
Outer boundary of the gas disc	3.5 kpc
Dark-halo mass, $M_h^{(Sat)}(r \leq 5\,\text{kpc})$	$0.372 \times 10^{10} \, M_\odot$
Initial azimuthal velocity, $v_{rot}^{(Sat)}$	$-9.45 \, \text{km s}^{-1}$
Initial radial velocity, $v_{rad}^{(Sat)}$	$-9.45 \, \text{km s}^{-1}$

Our calculations were performed in a Cartesian coordinate system, the center of which was determined by the center of the main galaxy. The initial plane of the MW disc coincided with the plane $z = 0$. We varied the following characteristics of the satellite: the gas mass $M_g^{(Sat)}$, the initial velocity and position of the center of the system, given by the distance to the center MW $r_0^{(Sat)}$, and the angle of incidence $\theta^{(Sat)}$ (Tables 1 and 2). The small angle $\theta^{(Sat)}$ corresponded to incidence from low galactic latitudes. The angle between the initial planes of the discs for the MW and the satellite was equal to $\beta^{(Sat)}$ ($\beta^{(Sat)} = 0°$ if the planes coincided; $\beta^{(Sat)} = 90°$ for perpendicular planes). We also considered models for comparison, in which both disc galaxies were gasless and in which the satellite was spherical. The models also differed in the radial profiles of their components. Physical characteristics in the work were used, both dimensional standard units (pc, $M_\odot$, year) and dimensionless ones, normalized to the following conversion scales: $\ell_M = 3.72 \times 10^{10} \, M_\odot$, $\ell_r = 9$ kpc, $\ell_V \simeq 133.7$ km s^{-1} and $\ell_t \simeq 63.2$ Myr [93].

More than 100 computational experiments have been carried out to study minor mergers. Table 2 contains the parameters defining the satellite models, which are discussed below. Fixed characteristics are specified in Table 1.

Table 2. Parameters of some numerical satellite models in addition to the constant characteristics in Table 1.

Name	$M_s^{(Sat)},$ $10^{10}\ M_\odot$	$M_g^{(Sat)},$ $10^{10}\ M_\odot$	$r_0^{(Sat)},$ kpc	$\theta^{(Sat)},$ degrees	$\beta^{(Sat)},$ degrees
G20	0.093	0.093	100.4	70.7	0
G21	0.093	0.093	128.5	11.3	0
G22	0.093	0	100.4	70.7	0
G23	0.093	0	128.5	11.3	0
G24	0.093	0.0465	128.5	11.3	0
G25	0.093	0.093	127.3	0	0
G27 (Sph)	0.093	0	128.5	11.3	–
G28 (Sph)	0.093	0	100.4	70.7	–
G30	0.093	0.093	100.4	70.7	90
G31	0.093	0.093	128.5	11.3	90
G41	0.093	0.093	128.5	11.3	0
G49	0.07	0.07	128.5	11.3	0
G50	0.085	0.085	128.5	11.3	0
G100	0.093	0	128.5	11.3	0

3. Simulation Results

3.1. General Picture of the Minor Merging Dynamics

The initial state of the system was chosen so that the satellite passed through the MW disc at the first pericentric approach and each next approach in the numerical experiment. Figure 3 shows the characteristic stages of the initial evolution of the stellar component of only the satellite in the process of minor merging at the following time points: (1) the pericentric approach of the satellite to the main galaxy (0.6×10^9 years); (2) the moment of the first impact (0.884×10^9 years); (3) the moment of maximum distance of the satellite from the MW after the first passage through the main disc (1.138×10^9 years); (4) the moment of the second impact (2.18×10^9 years); (5) the maximum distance of the satellite's core from the MW after the second impact (2.402×10^9 years). The dwarf galaxy in the experiment "G21" fell at a low angle of incidence $\theta^{(Sat)}$. This satellite trajectory disturbed a noticeable part of the MW disc, with gas ejected above and below the disc (Figure 4).

We do not depict the stars of the main galaxy in Figure 3, which lie within approximately 6 radial scales $r_d^{(MW)}$ for the entire simulation time of 9.5 billion years. This area is highlighted by a white circle with a radius of 12.5 kpc in Figure 3. Only a very small fraction of MW stars were ejected from the original disc, forming a thick disc and part of the stellar halo. The core of the satellite is clearly visible in yellow with maximum density, surrounded by red and blue areas with lower concentration in Figure 3. This core was stripped off with each passage through the main disc, due to the loss of primarily external particles. As a result, a compact elliptical stellar system began to form. We will also use the term "satellite core" (SC) to refer to proto-cEs/UCDs at various stages of evolution.

The initial size of the gaseous disc was approximately twice the size of the stellar disc, which enhanced the efficiency of the impact interaction between the satellite gas and the host galaxy, due to the collisional nature of the gaseous component (Figure 4). The satellite lost a noticeable portion of its gas during the first crossing of the MW disc, throwing gas from the main galaxy out of the disc to a height of up to 10 kpc in both directions. This gas then settled onto the disc. Tidal thin gas bridges and tails are clearly visible in Figure 4.
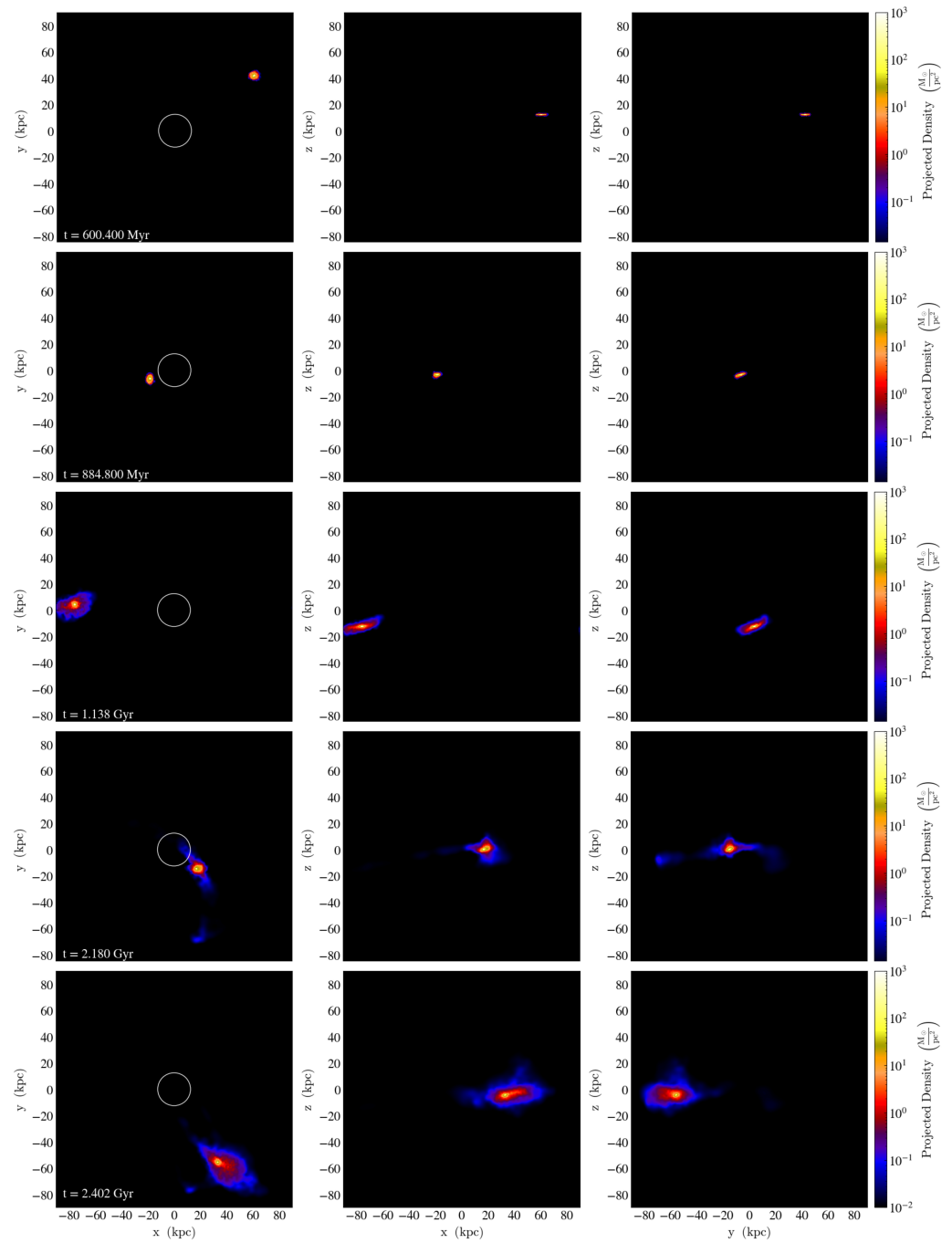
Figure 3. Density distributions of the satellite stars along the line of sight $\Sigma_s^{(\ell)}$ in three projections at five consecutive times ($t = 0.60, 0.88, 1.14, 2.18, 2.40$ billion years) for the "model G21" (see Table 2). The white circle shows the radius where the stellar disc of the main galaxy is located.
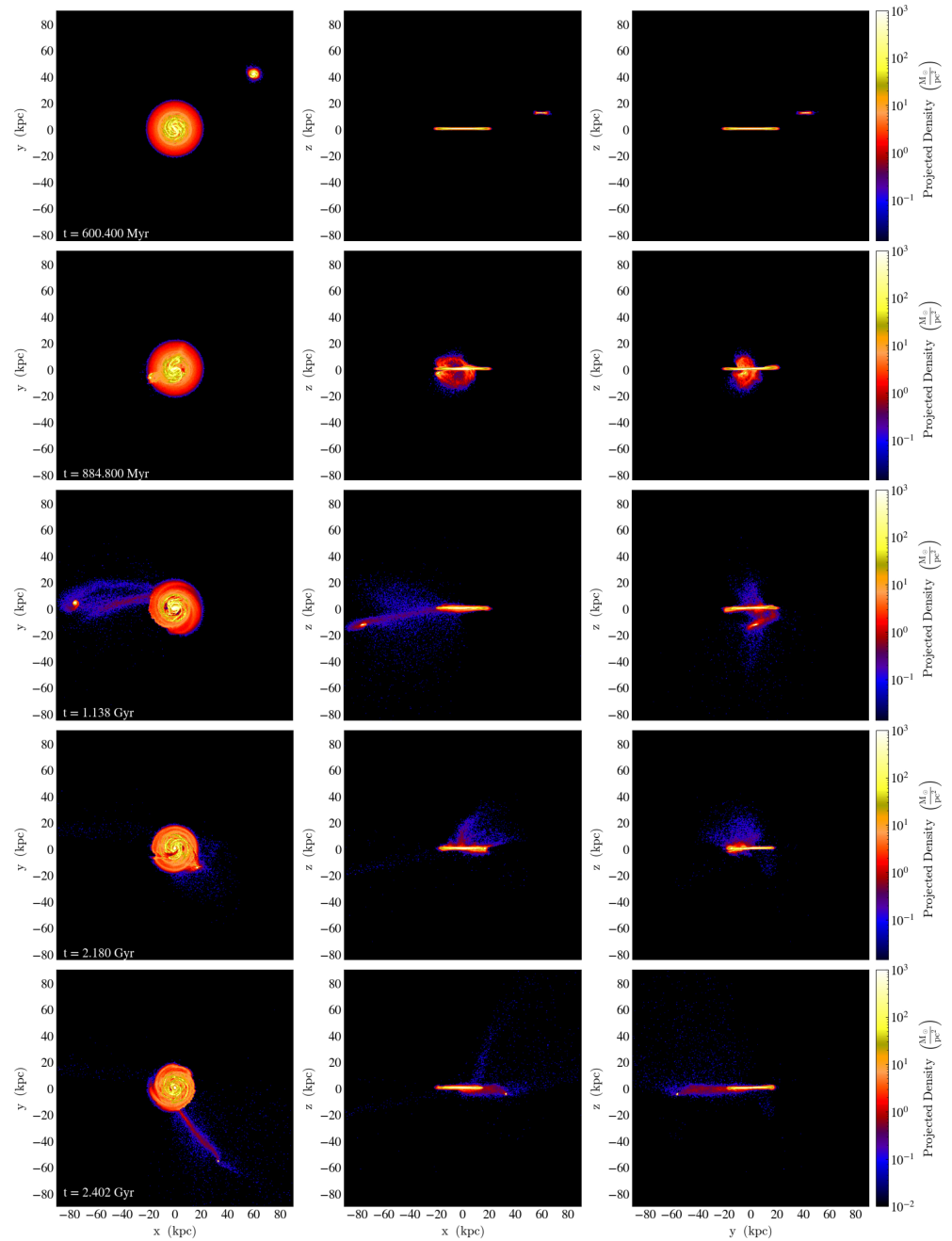
Figure 4. Density distributions of the total gas of two galaxies along the line of sight $\Sigma_g^{(\ell)}$ in three projections at five consecutive times for the model "G21", as in Figure 3.

The further evolution of merging after 2.4 billion years is shown in Figures 5 and 6. Three similar projections of the densities of stars ($\Sigma_s^{(\ell)}$) and gas ($\Sigma_g^{(\ell)}$) are given at five times: (1) fourth crossing of the disc (3.634×10^9 years); (2) maximum distance of the satellite core from the MW after the fourth impact (3.855×10^9 years); (3) fifth impact (4.203×10^9 years); (4) maximum distance of the core after the fifth passage (4.424×10^9 years); (5) the final stage of evolution in the numerical experiment after the 15th passage (9.29×10^9 years). We see the continuation of the destruction of the stellar component of the satellite with the formation of a compact dense core. Such a core is clearly visible in the bottom panel of Figure 5 near the point with coordinates ($x = -34$ kpc; $y = 25.4$ kpc; $z = 3.5$ kpc), which we treat as an object of type UCD/cE.

The stellar halo of minor galaxy stars around the MW disc became denser as the dwarf galaxy was stripped away. The oblateness of the inner stellar halo was due to the

features of the initial trajectory of the satellite, which invaded the main disc from low latitudes, $\theta^{(Sat)} = 11.3°$ (see Figure 3). The formation of new stellar streams weakened after 4–5 billion years, as the rate of stars lost to the SC decreased greatly (see below). At later stages, traces of flow structures are clearly visible, which reflects the history of the merger (see, for example, the top view in the plane $(x; y)$ at time $t = 9.29$ Gyr in Figure 5). Various substructures stand out most clearly according to the results of analysis in phase space (see, for example, [74,83,88,89,115]).
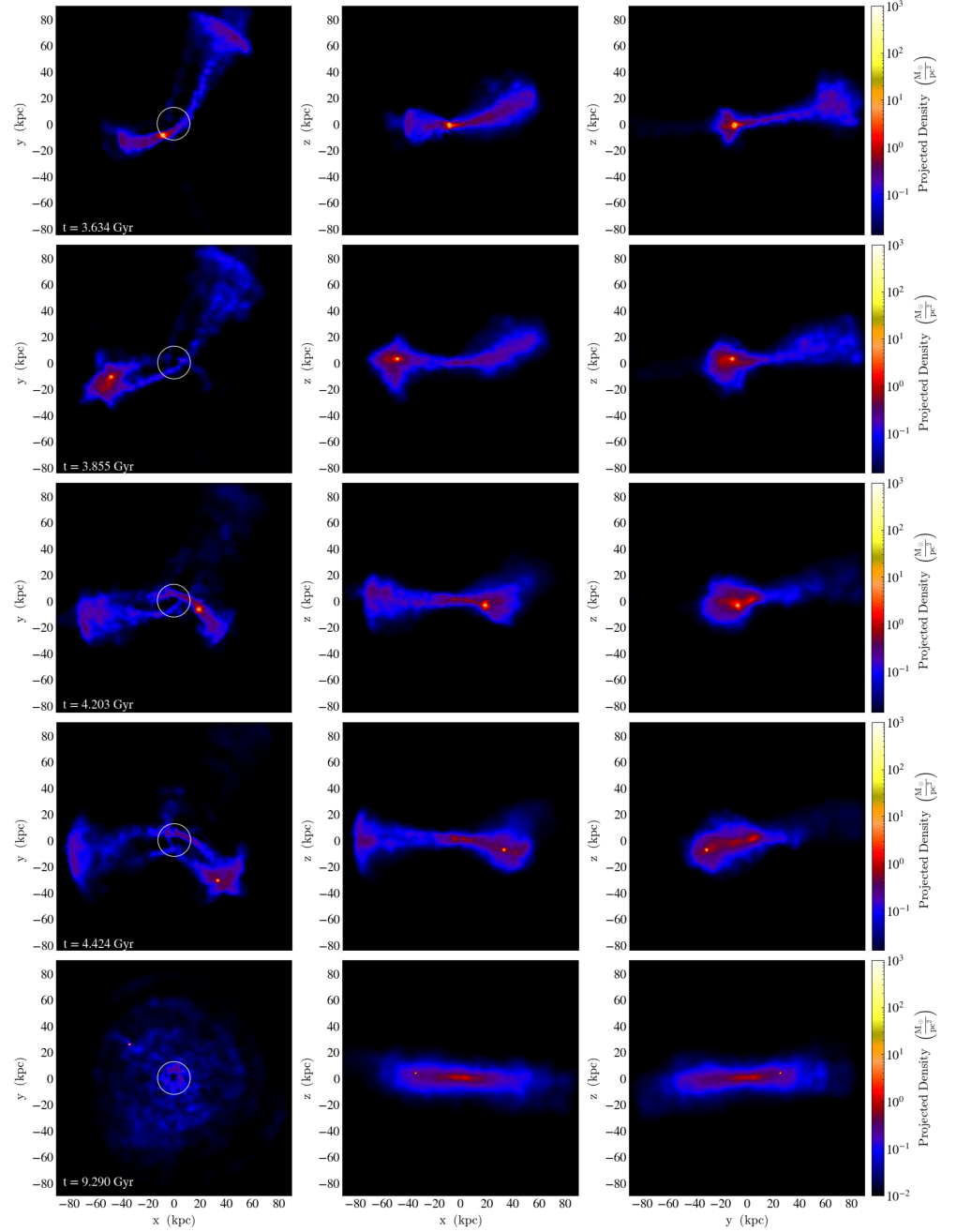

Figure 5. Density distributions of the satellite stars along the line of sight $\Sigma_s^{(\ell)}$ in three projections, as in Figure 3, at subsequent times (model "G21").
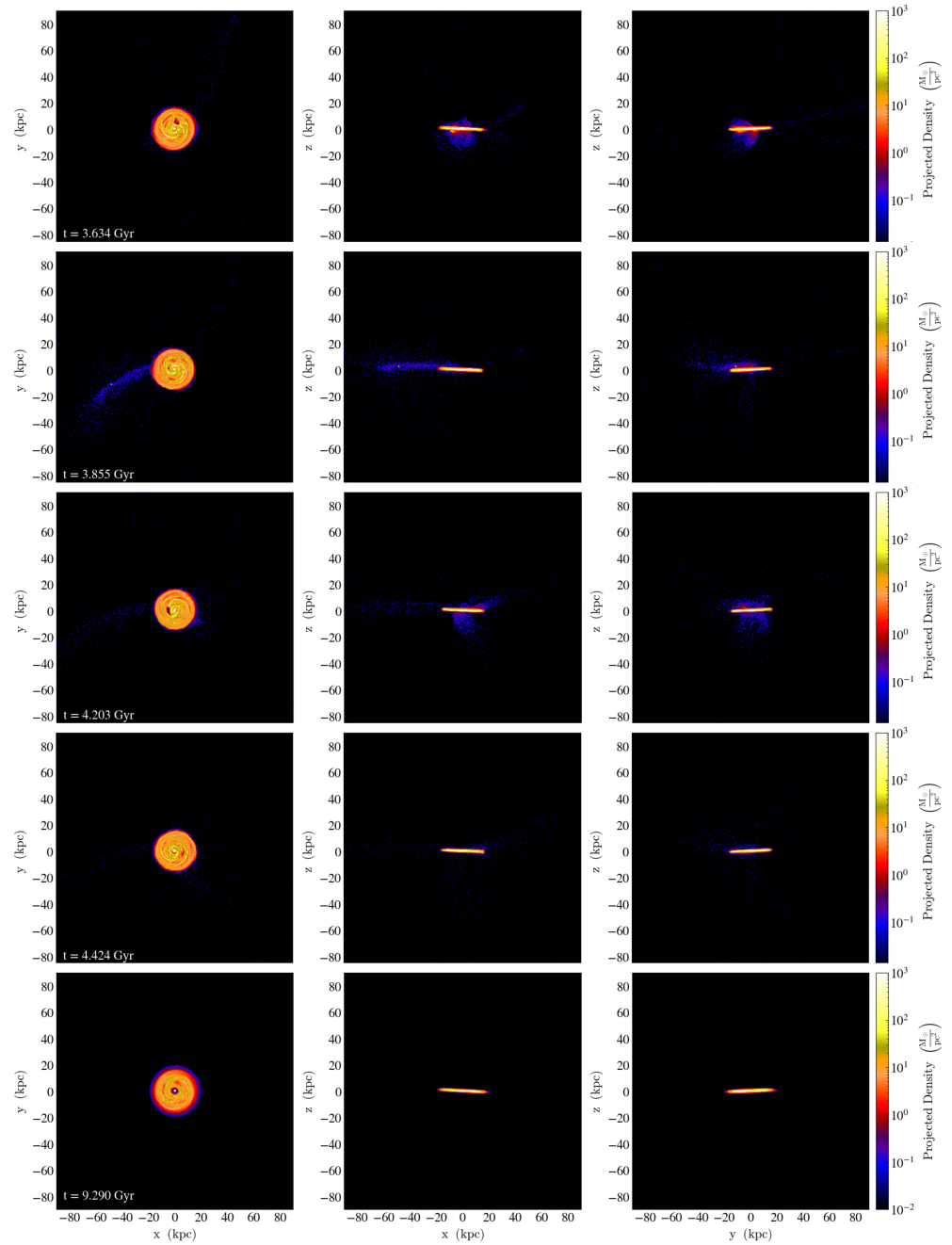
Figure 6. Gas density distributions, as in Figure 5 (model "G21").

Figure 6 shows the gas density along the sight line at long times in accordance with the distribution of the stars in Figure 5. The density $\Sigma_g^{(\ell)}$ at $t = 3.855$ Gyr still highlights the noticeable presence of gas in the SC (compare the yellow spots with coordinates $(x = -53\,\text{kpc}; y = -10\,\text{kpc}; z = 3\,\text{kpc})$ on the corresponding panels in Figures 5 and 6). At large times, the gas actively left the SC, as the density of the gas in the core decreased compared to the gas in the MW, and as the gravitational well of the satellite core was shallow compared to that created by the MW disc. The gas disc of the main galaxy effectively cleared the SC of gas at each crossing. As a result, the gas component of the satellite was almost completely absorbed by the MW gas disc after 4 Gyr under the conditions of the model "G21", which is typical for other models studied. Only a very small fraction of the gas ended up in the intergalactic medium, ranging around 1 percent in different models over long periods of time.

Figure 7 shows the distribution of the companion's stellar component in three projections after the third passage through the disc of the main galaxy. These images demonstrate the influence of model parameters on merger dynamics. The two basic models "G20" and "G21" initially contained a lot of gas and differed only in their initial fall trajectories at close-orbital-eccentricity values. The angle of attack in the first model was close to normal ($\theta^{(Sat)} \simeq 71°$), and the second model had $\theta^{(Sat)} \simeq 11°$ (see Table 2). We compared these two models to the corresponding calculations without gas (models "G22" and "G23"). These pictures show the influence of the gas in the satellite on the dynamics of the merger. The pair of models "G21" and "G23" provided a noticeable braking effect from the gas, as the core in the "G23" went to a maximum distance from the MW center of 101 kpc instead of 59 kpc for the "G21" (compare the first and second rows in Figure 7). Similarly, the difference between the pair of simulations "G20" and "G22" was 68 kpc and 83 kpc, respectively.
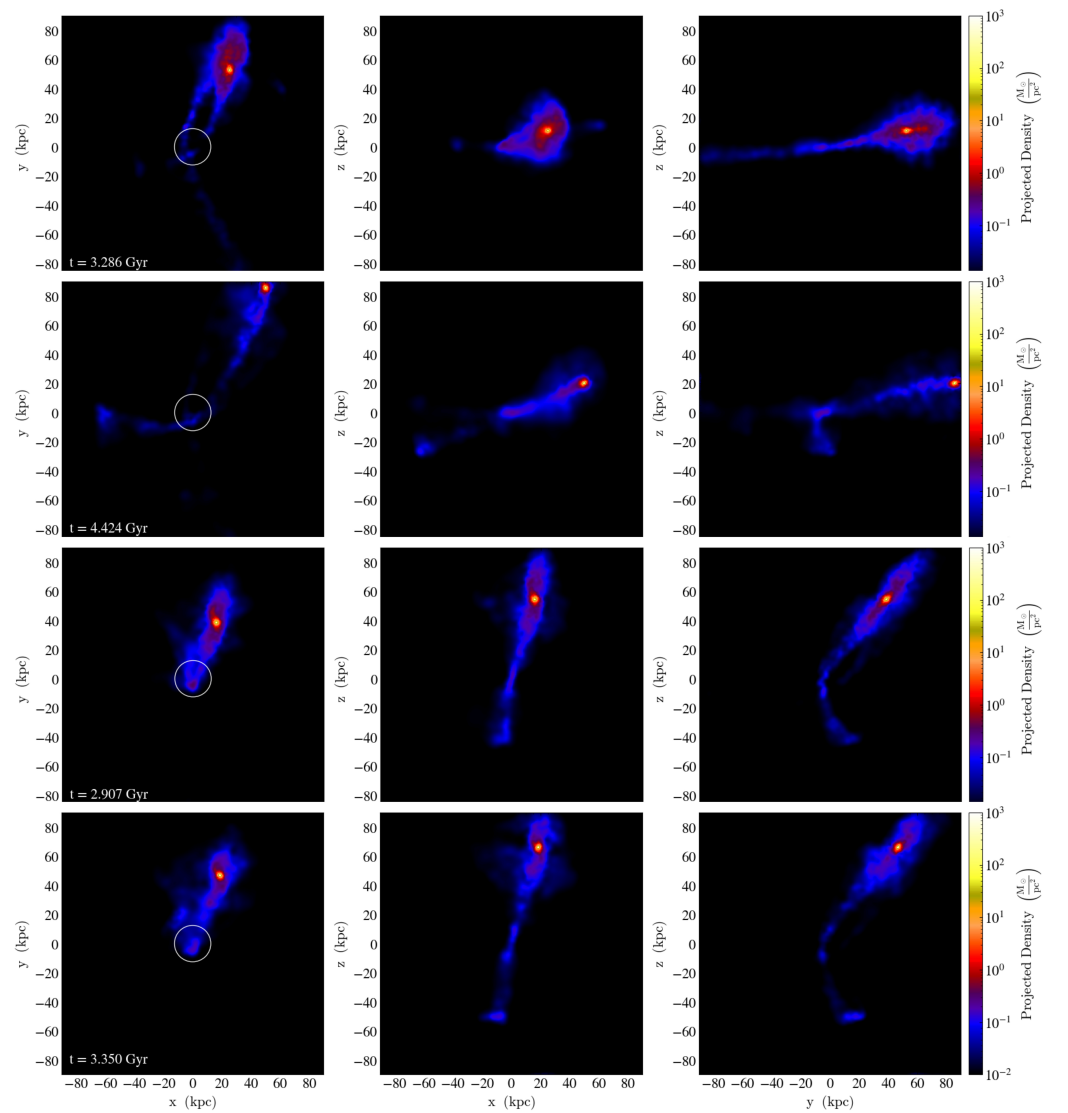

Figure 7. Star density distributions of the satellite $\Sigma_S^{(\ell)}$ after the third crossing of the MW disc at maximum SC distance for four models: (1) "G21" (**top**); (2) "G23" (**second row**); (3) "G20" (**third row**); (4) "G22" (**bottom**).

3.2. Formation and Characteristics of Transitional cE/UCD

We will consider in more detail the properties of the satellite's cores, which stand out in Figures 3–7, in the form of small yellow spots. Their masses and sizes fell within the

range between small compact elliptical galaxies (cEs) and the largest ultra-compact dwarf galaxies (UCDs), which are classified as the transitional UCD/cE type.

The first problem was related to isolating the size of the satellite's core in a numerical model throughout its evolution. The SC center was determined by the density maximum at some point $\vec{r}_C$, as seen in Figures 3–6. We calculated the mass inside spheres centered at $\vec{r}_C$ with different radii R_C as a function of time. Such time dependencies of the mass $M_C(t; R_C)$ are shown in Figure 8a and were typical for all models. Passages of the SC through the main disc are clearly marked by jumps in the dependencies $M_C(t)$, especially for large radii R_C (see Figure 8a). The lost mass in the core was higher at the first crossing and decreased with time. The determination of the effective core radius $R_C^{(eff)}$ contained some uncertainty, due to differences when using either the bulk density of matter in the core ($\varrho_C(r)$) or the surface density along the sight line ($\Sigma_s^{(\ell)}$). We assume below that within the radius $R_C^{(eff)}$ is half the mass based on bulk density calculations (Figure 8b). We also highlight the radius in Figure 8b, within which 3/4 of the SC mass is located.
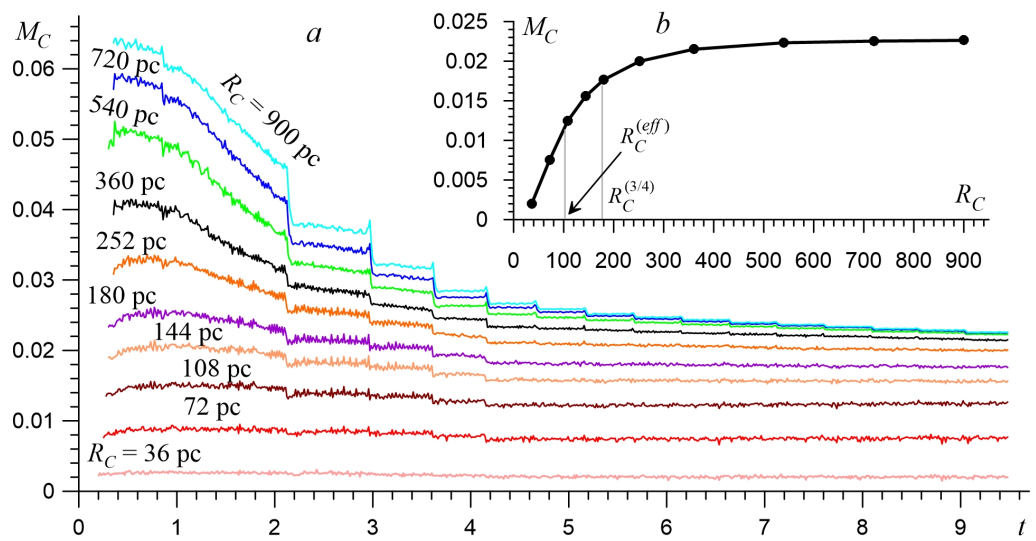

Figure 8. (**a**) Mass of stars in the SC ($[M_C] = 10^{10}\,M_\odot$) inside a fixed radius ($[R_C] = $ pc) vs. time in the model "G21" with high initial gas content. (**b**) Mass of stars inside the sphere with radius R_C for the final state ($t > 9 \times 10^9$ years).

Figure 9 is analogous to Figure 8 for the model "G23" in the initial absence of gas in the satellite. The efficiency of core mass loss was reduced by approximately 2 times. As a result, the final size $R_C^{(eff)}$ (or $R_C^{(3/4)}$) and the corresponding core mass M_C were approximately 2 times larger. Narrow peaks on the functions $M_C(t)$ at the moments of passage of the core through the disc were determined by the geometric factor, as the stellar mass of the main galaxy also fell inside the fixed sphere R_C. The time of such particles' velocity inside the core was short, and they quickly left the radius R_C, as there was no gravitational connection, due to very different kinematic characteristics (see, for example, the curve for $R_C = 1260$ pc in Figure 9a).

The considered minor merger led to the formation of a compact/ultra-compact elliptical-type star system from a dwarf spiral galaxy. Simulation of the interaction of a satellite without gas gives a more massive and larger core for a given initial mass of the stellar component $M_s^{(Sat)}$. The presence of gas can create a more compact core. Approximately 30–50 percent of the satellite's stellar mass goes towards building the elliptical core. The rest of the matter scatters, forming primarily a stellar halo around the main galaxy.
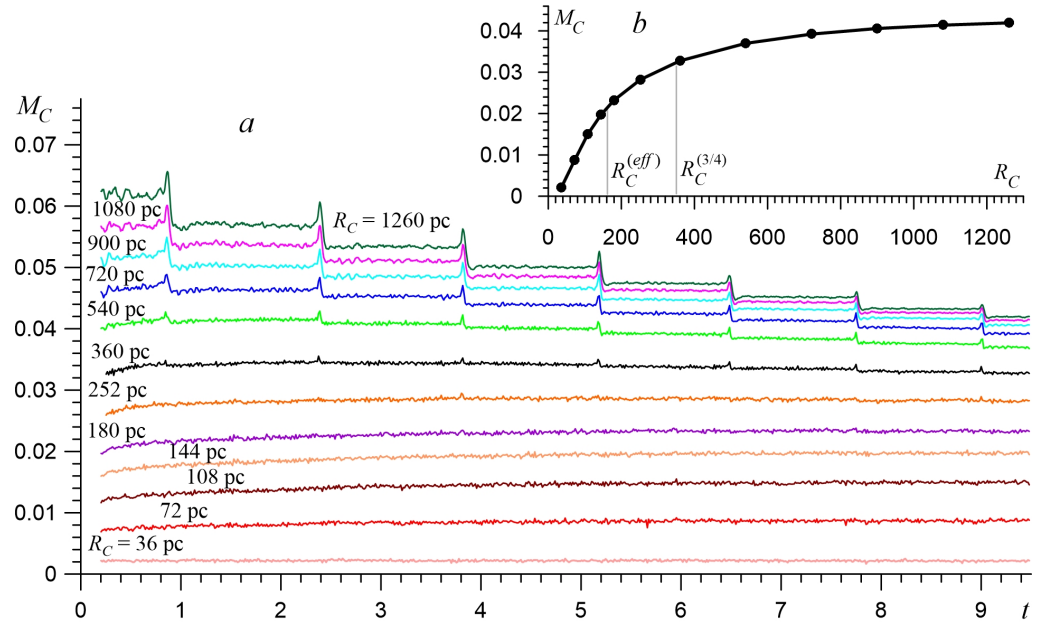
Figure 9. As in Figure 8 for the model "G23" without gas. (**a**) Mass of stars in the SC inside a fixed radius vs. time in the model "G23". (**b**) Mass of stars inside the sphere with radius R_C for the final state ($t > 9 \times 10^9$ years).

Figure 8 gives a visual representation of the mechanism of core stripping due to interaction, when mass loss occurred due to the outer layers of the core. The mass decreased most dramatically during approximately the first 4 billion years, within the sphere of 300–900 ps. Then, the SC mass almost stopped changing, so the effective radius was approximately $R_C^{(eff)} \simeq 100$ pc and 3/4 of the mass was inside $R_C^{(3/4)} \simeq 180$ pc. The dependence in Figure 8b shows the mass content M_C inside a sphere of radius R_C in the interval t = 9–9.5 billion years, highlighting the radii $R_C^{(eff)}$ and $R_C^{(3/4)}$.

The satellite contained three components (stars, gas, and dark mass), which reacted differently to the process of interaction with the main galaxy over 10 billion years (Figure 10). The times of crossing of the disc were well recorded by characteristic jumps of decreasing mass inside a sphere with a given radius. The satellite's gas was retained within the core after three passes through the MW disc in the model "G21" (see the red line in Figure 10b). The fourth crossing swept away gas almost completely from the core. The fall of the satellite from high galactic latitudes in the model "G20" could preserve gas in the core for longer times (Figure 10a). There was an effect of a secondary increase in the mass of gas in the core after passing through the main disc, due to the capture of matter at high galactic altitudes. The mass of gas in the core (red curves in Figure 10) sharply decreased when the core collided with the disc and then quickly increased to an approximately constant level until the next interaction event. Real capture of gas from the main galaxy by the core was possible with different merging parameters (see green lines in Figure 10). However, the mass of MW gas in the core of the satellite was very small at all stages of evolution. The narrow upward peaks in the dark mass were a consequence of the geometric method of calculating M_C, as in the case of the stellar component. It must be emphasized that the masses in Figure 10 were calculated inside spheres of large radius, where almost all of the gravitationally bound mass of the core was guaranteed to be located. The effective radii $R_C^{(eff)}$ were noticeably smaller than the considered values (see Figures 8 and 9).
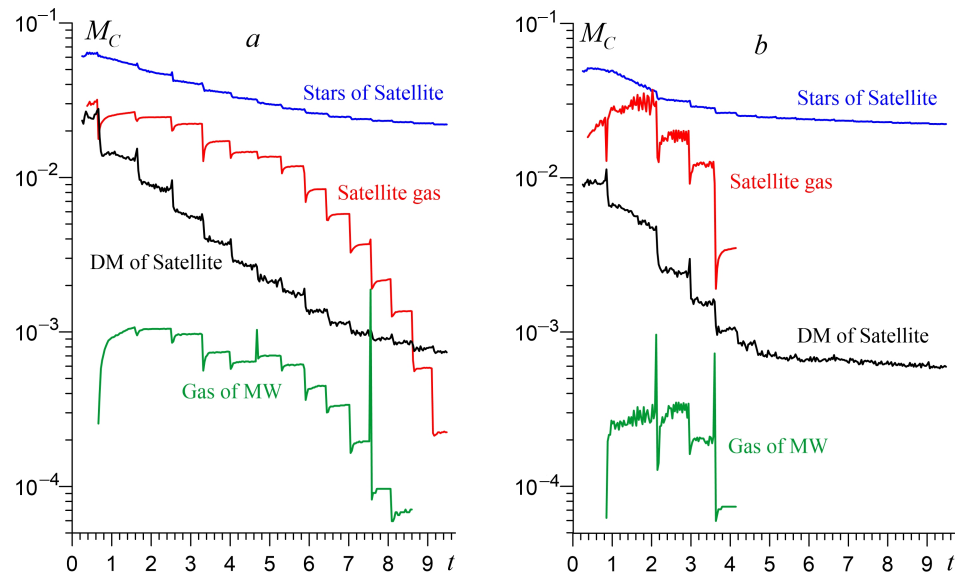
Figure 10. Masses of various components of the forming SC as a function of time in the models "G20" with $R_C = 900$ pc (**a**) and "G21" with $R_C = 540$ pc (**b**).

The dark mass did not have a significant effect on the dynamics of the SC formation (see the black curves in Figure 10) and, as a result, the formed compact star system contained a small percentage of the dark mass. The black solid line shows the DM within 900 pc, and the dotted line was calculated for a sphere with a radius of 5 kpc, which determined the region of the initial location of dark matter in the satellite. As we can see, the rate of DM loss was maximum compared to stars and gas.

The trajectories of the core were complex, due to the heterogeneity and asymmetry of the gravitational potential. The distance between the centers MW and SC was equal to r_C. The function $r_C(t)$ was characterized by a maximum distance ($r_C^{(max)}$, apocenter) and a minimum value ($r_C^{(min)}$, pericentric approach), indicating the radius in the MW disc at which the core crossed through the disc (Figure 11). The dependencies in Figures 10 and 11 clearly distinguish two stages of evolution of the distance $r_C(t)$ in the models with a large gas content (models "G20" and "G21"). There was a rapid decrease in local maxima, initially in the presence of gas. The decrease in $r_C^{(max)}$ slowed down significantly after the fourth MW crossing. The role of gas is shown in Figure 11, where the dependencies $r_C(t)$ are compared in pairs for the models "G20"–"G22" and "G21"–"G23". The difference in gas content in the satellite models led to a strong change in the trajectory, due to the sweeping of gas from the SC. Models without gas (dashed lines) gave small changes in the maximum core distance $r_C^{(max)}$ from the MW center over 9 Gyr. The gas-rich satellite (solid lines) moved in a more limited region and $r_C^{(max)}$ was 50–60 percent smaller compared to models without gas.

The passage periodicity of the satellite's core through the disc of the main galaxy was characterized by the time τ_C, which depended on the model parameters and changes during the computational experiment (Figure 12). The values of τ_C at the first impacts depended primarily on the initial parameters of the model, $r_0^{(Sat)}$, $v_{rot}^{(Sat)}$, $v_{rad}^{(Sat)}$, $\theta^{(Sat)}$ (see Tables 1 and 2). The general trend was a reduction in the time interval τ_C after the interaction event due to the loss of total energy, which strongly depended on the gas content in the dwarf galaxy.

The period τ_C changed slightly after gas loss at times $t \gtrsim 4$ billion years (the solid lines in Figure 12). The frequency of the disc crossing by the core was significantly lower in models that were initially without gas (dashed lines).
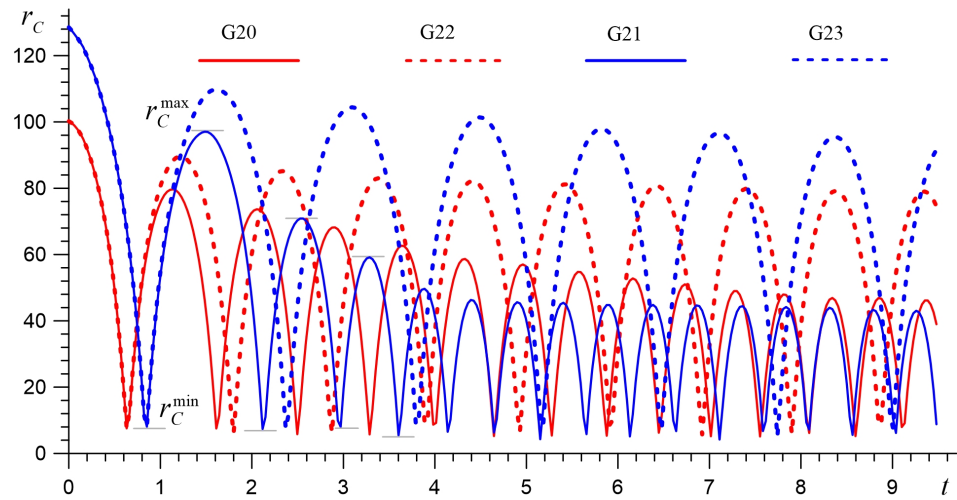
Figure 11. Dynamics of distances between the SC and MW centers, $[r_C] = \text{kpc}$, $[t] = \text{billion years}$.
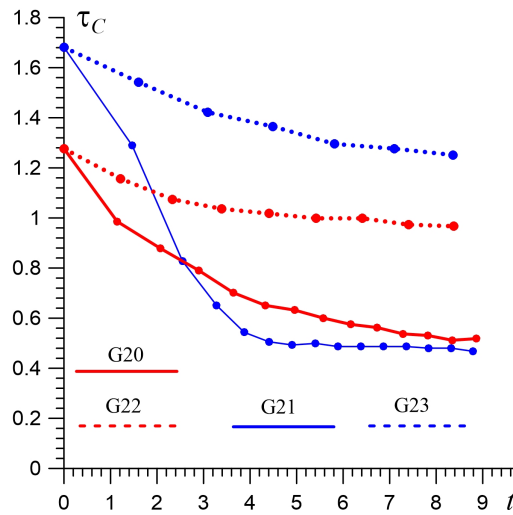

Figure 12. Periodicity of the passage of the core through the main disc vs. time in different models.

The process of formation of the elliptical core and peeling of the outer layers was accompanied by a decrease in the specific angular momentum $L_C(t)$ ($[L_C] = \text{kpc km s}^{-1}$, Figure 13a). Thus, the value of L_C decreased due to a decrease in both the size of the core and the internal rotation velocity of the stellar component. After 4 billion years, the core had an almost ellipsoidal shape and a rotation velocity of several kilometers per second, which was approximately an order of magnitude less than the velocity dispersion of the stars. This result is typical for models with rich initial gas content. Figure 13b shows the evolution of model "G23" without gas, for comparison. The rate of angular momentum loss was significantly less, so that a noticeable part of the kinetic energy was associated with the system rotation. The curves in Figure 13a clearly show that angular momentum was lost as a result of the first four passages of the SC through the main galaxy. Then, the gas was almost completely swept out of the core (see Figure 10b), and the loss of angular momentum occurred slowly. We calculate the rotation curve $V(r)$ for the core using the specific angular momentum based on the formula $V(r) = \dfrac{1}{r} \dfrac{dL_C^{(tot)}}{dr} \left(\dfrac{dM_C}{dr} \right)^{-1}$, where $L_C^{(tot)}$ is the total angular momentum (Figure 13c). This simple approximate method of constructing the rotation curve already shows the differences between the models "G21" and "G23".
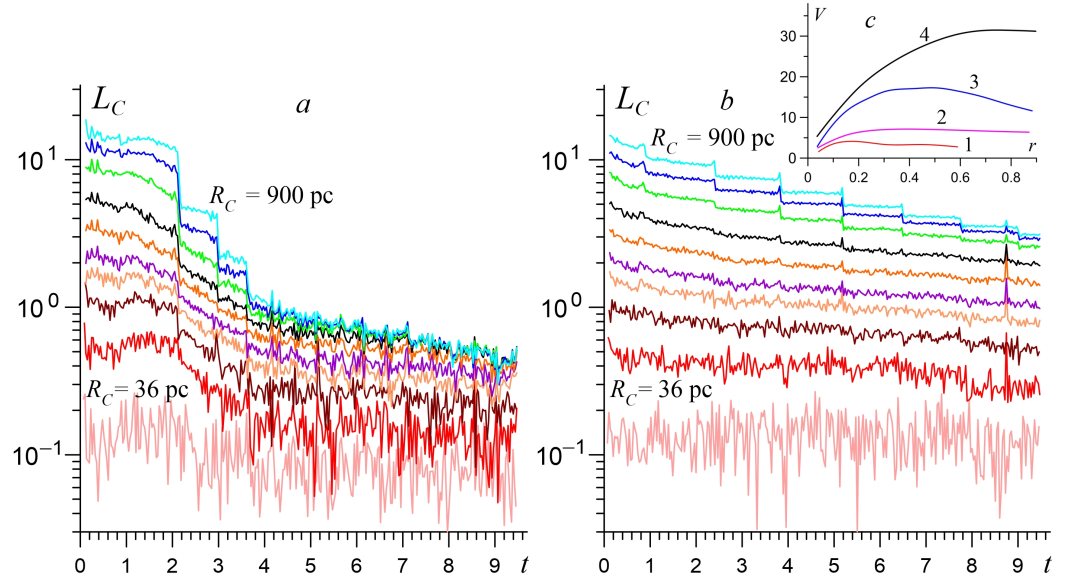
Figure 13. Specific angular momentum of the SC (L_C) inside different radii vs. time in the models "G21" (**a**) and "G23" (**b**). The line colors correspond to the conditions in Figure 8, where the radius R_C varies from 36 pc to 900 pc. (**c**) Rotation curves of the SC, reconstructed from the total angular momentum $L_C^{(tot)}(r)$: the model "G21" (curve 1 for the SC at the end of evolution, curve 2 was after the formation of SC); the model "G23" (3—SC at the end of evolution, curve 4 after the SC formation); $[V] = \mathrm{km\,s^{-1}}$.

Figure 14a summarizes the behavior of the total gravitationally bound core mass in different models. All the curves characterize the mass within 900 pc over 9 billion years. We see characteristic stepwise decreases in mass when crossing the MW disc. Mass loss from the core outside the main galaxy disc was small, except in models with gas, when there was a noticeable decrease in the stellar mass in the SC at high altitudes above the main disc. This effect is clearly visible in model "G21" at $t < 3$ billion years and in model "G20" until approximately 5 billion years. This difference was due to the fact that the SC in the "G20" retained gas longer than the model "G21" (see Figure 14a). The sequence of three curves $M_C(t)$ for models "G21" (a lot of gas), "G24" (gas halved), and "G23" (without gas) clearly shows the influence of the gas component on the formation of the compact-stars system. The model "G30" was an analogue of the "G20" except for the initial orientation of the satellite's disc, which was perpendicular to the disc of the main galaxy. This had little effect on the dynamics of tidal disruption/stripping of the satellite (see the black line in Figure 14a).

A feature of the studied models of minor merging was the presence of the gas and stellar discs in the satellite with a sufficiently powerful stellar bar before the destruction of such a small galaxy begins. Figure 14b shows the distributions of stellar and gas components in the model "G21" before the first impact, which are typical for all the models considered here. Analysis of the trajectories of all particles led to the conclusion that the SC was formed primarily from the material of the central region of the stellar bar. The complex rotational motions of the bar particles were destroyed by tidal interactions, and the resulting compact elliptical system retained only a weak relict rotation. The typical ratio of the minor to the major axes was close to 0.85 at the end of evolution.

A significant result is that the formed stellar cores of the transitional cE/UCD type are long-lived objects under conditions of periodic flights through a massive large galaxy and can exist for cosmological timescales.
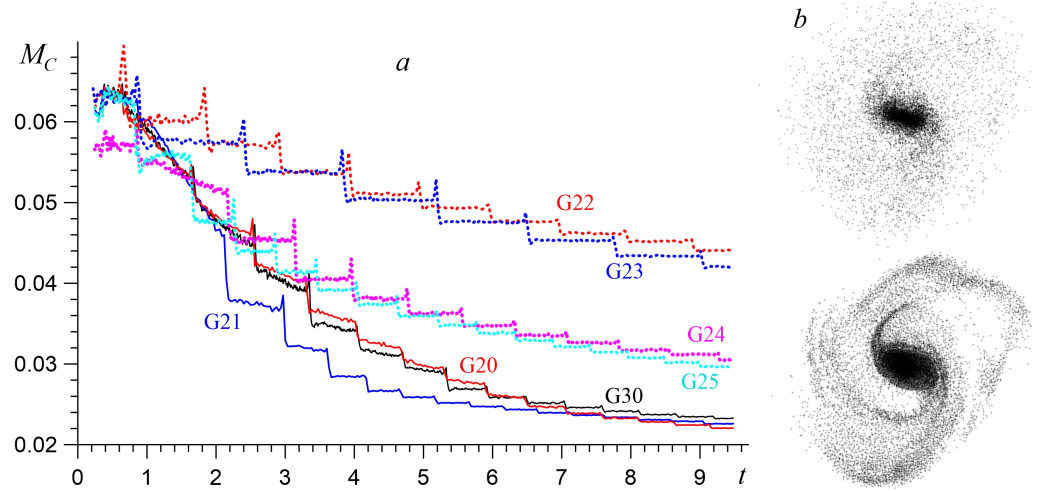
Figure 14. (**a**) Dependence of the total stellar core mass on time in different models. (**b**) Stellar (top) and gas (bottom) discs of the satellite before their first passage through the MW (model "G21").

The final mass of the SC is determined by the initial mass of the satellite and its radial initial stellar density profile. This issue requires some further consideration. Models "G20"–"G25" and "G30" (see Figures 8–14) contained massive concentrated nuclei. Mass density in the central region was low in models "G46", "G49", "G50", and "G100". Figure 15 shows the differences in mass loss rates between the models "G100" and "G23" (see Figure 9), due to the lack of an initial concentrated core in model "G100". The decrease in mass M_C inside a sphere of fixed radius R_C was several percent at the periphery and did not affect the core region of the model "G23" at long times. The model "G100" was distinguished by the absence of an initial concentrated core, which resulted in a strong stripping of the entire stellar component at all radii throughout the entire evolution (Figure 15a). Figure 15b shows the radial dependencies of the mass inside a sphere with radius R_C, as in the corresponding Figures 8b and 9b. Such an SC was too loose compared to the observed UCDs. If the mass $M_C \simeq 3.2 \times 10^8 \, M_\odot$ with an effective radius $R_C^{(eff)} = 450$ pc at time 4.5×10^9 years allowed us to attribute an object to cE type, then the SC mass decreased greatly after 3 billion years with an almost constant effective radius. Thus, the model "G100" was an example of the complete destruction of an object of type cE. The SC evolved in a similar way in the models "G49" and "G50".
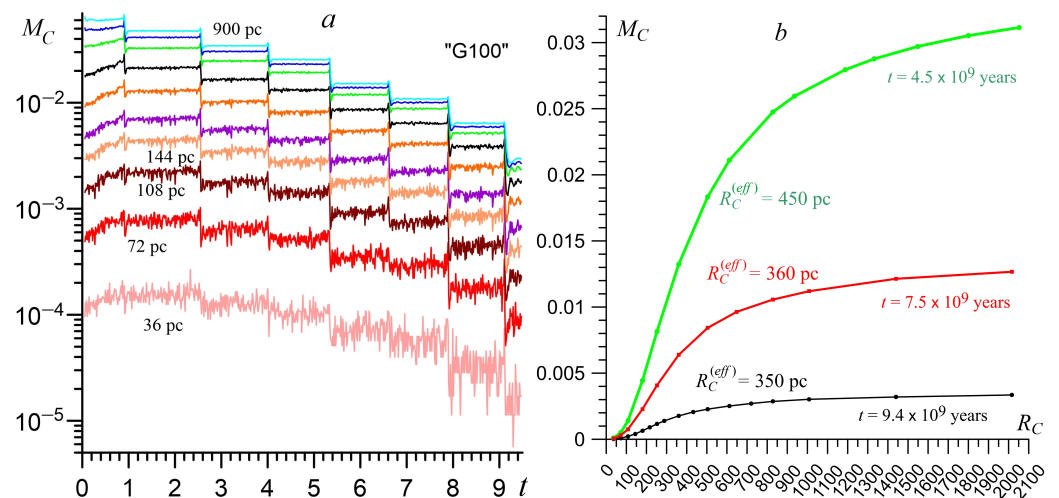

Figure 15. (**a**) As in Figure 8 for the model "G100". (**b**) Mass of stars inside the sphere with radius R_C at different times (model "G100").

Let us discuss the radial distributions of the surface density of stars ($\sigma_s^{(SC)}(r)$) in SCs as corresponding to the observed characteristics along the line of sight. Figure 16 shows such dependencies on the radius r for some models. For example, profiles $\sigma_s^{(SC)}(r)$ for the model "G21" are shown in Figure 16a. The red color shows density distributions after the fourth crossing of the MW. We presented several dependencies at different times from the interval t = 3.8–4 billion years, to show local changes in quantities. Half of the SC's mass for surface density $\sigma_s^{(SC)}(r)$ was inside the effective radius $r^{(eff)}$ = 97 pc. The value of $r^{(eff)}$ decreased to 68 pc, due to the stripping of the outer layers after the 15th crossing of the host disc (blue circles in Figure 16a). The inner part of the surface density profile (<100 pc) remained almost unchanged. Two characteristic zones were distinguished. Both were well approximated by exponential laws with different radial scales. Figure 16b shows the model "G23", as an analogue of the "G21" without gas, and the model "G41", which formed a satellite core with a lower mass compared to the model "G21".
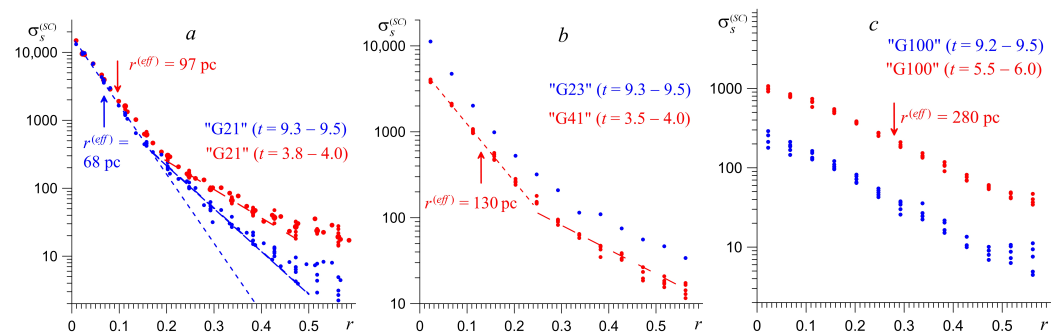

Figure 16. Radial profiles of surface density in SCs for different models (circles of different colors): (**a**) "G21" at two time intervals; (**b**) "G23" and "G41"; (**c**) "G100" at two time intervals. The lines correspond to exponential distributions. The arrows indicate the effective radii for the corresponding models.

Finally, Figure 16c contains profiles for models without an initial concentrated core in a dwarf galaxy. Four passes through the main disc reduced the SC's mass to $2.28 \times 10^8 \, M_\odot$ with an effective radius $r^{(eff)}$ = 280 pc. The stars content in such an object decreased rapidly. The seventh crossing of the host galaxy left approximately $5.5 \times 10^7 \, M_\odot$ in the SC at $r^{(eff)}$ = 383 pc, which was not typical for a UCD type. The model "G49" with gas without the initial concentrated nucleus left even less mass in the SC with a large effective radius. We limited ourselves to constructing the radial distributions of the surface stellar mass density $\sigma_s^{(SC)}(r)$ in Figure 16. The transition to surface brightness profiles could be made taking into account the observed mass-to-light ratios ($\mathcal{M}/\mathcal{L}$), which were $(\mathcal{M}/\mathcal{L})_B = 3 \, (M_\odot / L_\odot)$, and $(\mathcal{M}/\mathcal{L})_V = 2.5 \, (M_\odot / L_\odot)$ (PEGASE.2 models) for the objects under consideration.

4. Discussion

The results of modeling the merger of a dwarf barred galaxy with a large Milky Way galaxy are described in detail here. We focused on the evolution of the satellite's dense core, which transforms into a small, compact elliptical star system as its outer layers are stripped away and its angular momentum is lost as it repeatedly passes through the host galaxy's disc. Our analysis of the conditions for the formation of compact and ultra-compact elliptical galaxies as a result of minor merging was not comprehensive, due to the very large number of free parameters, the variation of which leads to significantly different classes of objects. Our efforts were aimed primarily at studying the influence of the initial gas on the efficiency of stripping the outer (less dense) layers of the forming compact core.

We considered two extreme classes of dwarf rotating galaxies. One contained a gas-rich disc with a mass comparable to that of stars. The second group of models did not contain gas, as in the case of dwarf lenticular galaxies (dS0s), in which gas does not

have a noticeable effect on the dynamics of the stellar component even in the presence of some star formation [116]. The baryonic mass of the dwarf galaxy model lay in the range $(1–2) \times 10^9 \, M_\odot$, which was significantly less than the disc mass of the host galaxy. The maximum circular velocity was 75–85 km s^{-1}, with the optical radius for the stellar component R_{opt} = 2.5–3 kpc.

The loss of a significant portion of the mass of a disc galaxy in the field of a massive elliptical galaxy at the center of a rich cluster was demonstrated in the work [13], where 75 percent of the mass was stripped by tidal forces. Our work was aimed at studying threshing in the field of a large spiral galaxy at large eccentricities of the satellite's orbit. Numerous passages of the dwarf through the disc of an MW-type galaxy were accompanied by the destruction of its structure and the loss of more than half of the stellar mass, which went towards the construction of a stellar halo around the main galaxy. The density distribution in such a stellar halo depends significantly on the galactic latitude of arrival of the satellite and is not centrally symmetric.

The formation problem of the galaxy vertical structure and stellar halo through the destruction of the Gaia-Sausage-Enceladus has been actively studied in recent years in connection with the outstanding data of the GAIA project [76,90,108,115,117]. The spatial picture of the dynamics of all gaseous and stellar components is complex. Therefore, the traditional approach to studying the consequences of merging is based on the properties of phase spaces—for example, energy, angular momentum, action, velocity components, and some other parameters [81,83,89,91,118,119]. Analysis of the phase distributions of spatial and kinematic characteristics for a large array of Gaia stars makes it possible to identify the history of interactions and mergings in the Milky Way. This method is applicable to data from the results of our minor merges simulations, and such studies are in our immediate plans.

Features of the satellite's trajectory significantly influence the merging process, and we are considering the most severe scenario of an almost radial fall, in contrast to a quasi-circular orbits. The lion's share of the satellite's gas is quickly captured by the MW gas disc, so that 1–2 percent of the gas ends up outside the main gas disc and becomes an intergalactic medium. This mechanism of enrichment of the intergalactic medium seems interesting for future research. The dwarf's initial dark mass becomes almost entirely part of the main galaxy's halo, with the shape of the additional dark halo generally close to that of the stellar halo.

The presence of gas appears to be an important factor in the birth of compact elliptical dwarfs, promoting the formation of a more concentrated core. The physical mechanism for more efficient stripping of the stellar component at an initial high gas content is as follows. The gas makes a noticeable contribution to the gravitational potential of the original dwarf before interaction. During the first and subsequent passages through the disc, the satellite can lose from 10 to 30 percent of the gas, which leads to a decrease in the depth of the gravitational well of the satellite's core. As a result, collisionless particles (stars and DMs) with large velocity dispersion are more easily stripped from the outer layers of the core, forming the stellar halo of the main galaxy.

The low content of dark matter in the core and around the core by the end of evolution (9.5 billion years) is determined, of course, by the initial DM profile in a dwarf galaxy, when the halo mass does not exceed the stellar component mass within the initial radius $R_{opt}^{(Sat)}$ and the radial scale of the dark halo is larger than the disc scale. The capture of dark matter by the stellar core hardly occurred in our numerical models, as even the stars of the main galaxy did not enrich the core of the satellite. The presence of dark matter in cEs depends on the initial DM radial density scale and, as it decreases, the fraction of dark matter in the core should increase. Paper [19] noted that the presence of a central cusp in a massive dark halo makes the formation of compact cores difficult. There are very different ratios of baryonic and dark matter among the observed zoo of cEs. For example, the galaxy PGC 029388 within $r^{(eff)}$ consists of 90 percent DM and is classified as a transition-type dSph-UDG with $r^{(eff)} = 1$ kpc [9]. Compact and ultra-compact elliptical galaxies can exist

over cosmological times despite strong tidal interactions. The lifetime of compact stellar cores in our models over several billion years was quite consistent with observational data and other numerical simulations [79,88,102,120,121].

A wide variety of baryonic-to-dark-matter ratios occur among observed cE galaxies. For example, the galaxy PGC 029388 inside $r^{(eff)}$ consists of DM of 90 percent and is classified as the transition-type dSph-UDG with $r^{(eff)} = 1$ kpc [9]. Compact elliptical galaxies can exist over cosmological times despite strong tidal interactions. The lifetime of compact stellar cores in our models is quite consistent with observational data and other numerical simulations [79,88,102,120,121].

We limited ourselves to models of a satellite with a small disc and a mass that produced a high concentration of stars in the central region of the disc. This contributed to the formation of more concentrated elliptical galaxies (cEs), which were close to UCDs. If the size of the satellite was increased—for example, to 6 kpc, like that of the Large Magellanic Cloud—while maintaining the baryonic mass of $2 \times 10^9 \, M_\odot$, then this would lead to a decrease in the mass of the core or to the complete destruction of the satellite in 9 billion years. The parameters of simulated dwarf elliptical galaxies approach those of ultracompact dwarfs. The construction of UCD models for a wide range of properties requires additional study. We plan to develop this study by varying the initial mass distribution of the stellar and gaseous discs in the satellite. A separate task is the fall of a dwarf galaxy without a bar. This initial model can easily be created by specifying a hotter stellar disc and/or a massive and concentrated dark halo. However, it is necessary to perceive that tidal forces are capable of generating a central bar when approaching the main galaxy.

The discovery of supermassive black holes at the center of compact dwarfs is an important factor in the dynamics of the entire compact star system, as the black hole's mass is noticeable compared to the UCDs [45–52]. The black hole helps maintain the rotation of the surrounding stellar component in the core and further increases the concentration of mass density as matter accretes onto the center. Including a supermassive black hole in the model of the original satellite for co-evolution during the stripping process could be significant. However, the numerical model used here did not allow us to qualitatively trace the dynamics on scales less than 1 pc. We must significantly increase computational resources to reliably simulate the formation of a cE/UCD with a black hole.

Another additional stripping mechanism may be associated with extragalactic hot gas. Ram pressure can effectively sweep gas out of the galaxy. Beautiful examples are jellyfish galaxies [122,123], from which gas comes out in a very long stream, due to ram pressure. Gas sweeping by ram pressure from the destroyed satellite changes the total gravitational potential. We showed in this work that this improves the efficiency of stripping the stellar component as well, as the gravitational attraction of the outer layers towards the center is weakened. Simulating minor merging to form compact star systems within hot, rarefied intergalactic gas could improve our understanding of the physics of these objects.

If we look at the GSE event in our galaxy, 10 billion years ago, the results obtained provide certain restrictions on the initial properties of the satellite in the MW. The presence of an increased concentration of stars in the center of a dwarf spiral galaxy before the merger began ensured the birth of a core with cE/UCD parameters. The system of small satellites in our Milky Way did not contain ultracompact or compact objects, which placed restrictions on the hypothetical Gaia-Sausage-Enceladus. The GSE did not appear to have had massive stellar core or bulge in the disc, as we did not see a suitable candidate for a compact or ultra-compact object as a remnant of the GSE.

5. Conclusions

We studied the possibility of the formation of compact elliptical galaxies (cEs/UCDs) as a result of a minor merger of a dwarf disc galaxy and a large Milky-Way-type spiral galaxy. Models of the satellite before interaction included stellar and gas components embedded in a dark halo. The maximum circular velocity of the satellite was typical for dwarf galaxies in the range of 75–85 $\mathrm{km \, s}^{-1}$ with an optical radius of about 3 kpc. The

model of the satellite before the collision contained a massive stellar bar and spiral pattern. The evolution of the interaction was simulated over a period of 9.5 billion years. Each pericentric approach of two objects occurred in the mode of crossing the stellar disc of the main galaxy by the satellite. This ensured the most severe destruction of the dwarf. The ratio of the total masses of two interacting galaxies in the models was 1/46–1/38 within the double optical radius of the stellar discs before the interaction began. This ratio is 1/30–1/60 for baryonic matter. The main attention was paid to the features of the formation of a long-lived compact core of the satellite, close to the characteristics of the transitional UCDc/cEs in mass and size.

The influence of gas on the process of loss of stellar mass by a satellite has been studied in detail. The loss of gas when crossing a large disc galaxy noticeably increases the stripping rate of the stellar component as well. The result of the studied minor merging is transitional cE/UCD galaxies with the following properties:

— Approximately half of the initial mass of stars can be used to build a compact stellar core. This fraction decreases with the increasing mass of gas in the satellite. The gas component is an important factor contributing to the stripping of the stellar and dark components when passing through the disc of the main galaxy. A gas-rich dwarf produces a compact core with 2 times less mass and size compared to the same satellite without gas. The final gas content in a compact object is negligible.

— The formation of a quasi-stationary compact core takes 4–9 billion years, depending on the gas content and the initial angle of incidence of the satellite on the disc. The fall of a gas-rich dwarf disc galaxy from a region of low galactic latitudes can create a cE/UCD galaxy in 4–5 billion years from just four or five disc crossings. The fall of a satellite from high galactic latitudes $\theta^{(Sat)}$ extends the time of formation of a compact elliptical galaxy.

— All the models gave strong stripping of the dark halo of the satellite. As a result, the DM mass decreased by more than an order of magnitude and did not have a noticeable effect on the dynamics of the satellite's core. Thus, the formed cE/UCD models did not contain significant dark mass at the end of the numerical simulations.

— The constructed models of compact elliptical galaxies differed slightly from the spherical shape, and the ratio of the axes gives the morphological type E0–E2, depending on the initial gas content in the satellite.

— The compact/ultra-compact cores in our numerical models have a mass of $(1\text{--}5) \times 10^8\, M_\odot$ and an effective radius of $r^{(eff)} = 60\text{--}200$ pc, and are long-lived. Such objects continue to persist almost unchanged over dozens of orbital periods, despite further numerous crossings of the disc of the main galaxy. The core stellar mass loss per revolution $\Delta M_C / M_C$ can initially exceed ~ 30 percent in gas-rich models and decreases greatly with each new crossing of the main galaxy. The result of one crossing of the disc by the core in the modern era after 9 billion years of evolution is $\Delta M_C / M_C \simeq 1\text{--}2$ percent in the initially gas-rich satellite and 3–6 percent in the gas-free satellite.

— The rotation of stars in stripped nuclei was determined by the initial gas content in the satellite in the considered models. A very gas-rich satellite produces cE/UCD-type objects with almost no rotation. Models without initial gas give noticeable internal rotation of the compact object. It should be noted that different mechanisms for stripping the nucleus of a dwarf galaxy can result in different rates of angular momentum loss. For example, our consideration of interaction with a large spiral galaxy may be very different from merging in a cluster with a cD galaxy.

Author Contributions: Conceptualization, A.V.K.; methodology, S.S.K.; software, S.S.K.; validation, D.S.S. and S.S.K.; formal analysis, A.V.K.; investigation, D.S.S. and S.S.K.; data curation, S.S.K. and D.S.S.; writing—original draft preparation, A.V.K.; writing—review and editing, A.V.K.; visualization, S.S.K. and D.S.S.; supervision, A.V.K.; project administration, A.V.K.; funding acquisition, A.V.K. All authors have read and agreed to the published version of the manuscript.

Data Availability Statement: Data are contained within the article.

Conflicts of Interest: The authors declare no conflict of interest. The funders had no role in the design of the study; in the collection, analyses, or interpretation of data; in the writing of the manuscript, or in the decision to publish the results

Abbreviations

The following abbreviations are used in this manuscript:

MW	Milky Way
GSE	Gaia-Sausage-Enceladus
DM	Dark Matter
SPH	Smoothed-Particle Hydrodynamics
UCDs	Ultracompact Dwarf Galaxies
UDGs	Ultra-diffuse galaxies
GCs	Globular clusters
NSC	Nuclear Star Cluster
SC	Satellite Core

References

1. Battaglia, G.; Nipoti, C. Stellar dynamics and dark matter in Local Group dwarf galaxies. *Nat. Astron.* **2022**, *6*, 659–672. [CrossRef]
2. Karachentsev, I.D.; Kaisina, E.I. New Local Volume Dwarf Galaxy Candidates from the DESI Legacy Imaging Surveys. *Astrophys. Bull.* **2022**, *77*, 372–387. [CrossRef]
3. Carlsten, S.G.; Greene, J.E.; Beaton, R.L.; Danieli, S.; Greco, J.P. The Exploration of Local VolumE Satellites (ELVES) Survey: A Nearly Volume-limited Sample of Nearby Dwarf Satellite Systems. *Astrophys. J.* **2022**, *933*, 47. [CrossRef]
4. Karachentsev, I.D.; Makarov, D.I.; Kaisina, E.I. Updated Nearby Galaxy Catalog. *Astron. J.* **2013**, *145*, 101. [CrossRef]
5. Chilingarian, I.; Cayatte, V.; Chemin, L.; Durret, F.; Laganá, T.F.; Adami, C.; Slezak, E. Discovery of a new M 32-like "Compact Elliptical" galaxy in the halo of the Abell 496 cD galaxy. *Astron. Astrophys.* **2007**, *466*, L21–L24. [CrossRef]
6. Chilingarian, I.V.; Prugniel, P.; Sil'chenko, O.K.; Afanasiev, V.L. Kinematics and stellar populations of the dwarf elliptical galaxy IC 3653. *Mon. Not. R. Astron. Soc.* **2007**, *376*, 1033–1046. [CrossRef]
7. McConnachie, A.W. The Observed Properties of Dwarf Galaxies in and around the Local Group. *Astron. J.* **2012**, *144*, 4. [CrossRef]
8. Henkel, C.; Hunt, L.K.; Izotov, Y.I. The Interstellar Medium of Dwarf Galaxies. *Galaxies* **2022**, *10*, 11. [CrossRef]
9. Afanasiev, A.V.; Chilingarian, I.V.; Grishin, K.A.; Makarov, D.; Makarova, L.; Fabricant, D.; Caldwell, N.; Moran, S. KDG 64: A large dwarf spheroidal or a small ultradiffuse satellite of Messier 81. *Mon. Not. R. Astron. Soc.* **2023**, *520*, 6312–6321. [CrossRef]
10. Makarova, L.N.; Makarov, D.I. Spatial segregation impact on star formation in nearby dwarf spheroidal galaxies. *Mon. Not. R. Astron. Soc.* **2021**, *502*, 1623–1632. [CrossRef]
11. Bekki, K.; Couch, W.J.; Drinkwater, M.J.; Gregg, M.D. A New Formation Model for M32: A Threshed Early-Type Spiral Galaxy? *Astrophys. J.* **2001**, *557*, L39–L42. [CrossRef]
12. Deeley, S.; Drinkwater, M.J.; Sweet, S.M.; Bekki, K.; Couch, W.J.; Forbes, D.A. The formation pathways of compact elliptical galaxies. *Mon. Not. R. Astron. Soc.* **2023**, *525*, 1192–1209. [CrossRef]
13. Chilingarian, I.; Cayatte, V.; Revaz, Y.; Dodonov, S.; Durand, D.; Durret, F.; Micol, A.; Slezak, E. A Population of Compact Elliptical Galaxies Detected with the Virtual Observatory. *Science* **2009**, *326*, 1379–1382. [CrossRef] [PubMed]
14. Newton, O.; Di Cintio, A.; Cardona-Barrero, S.; Libeskind, N.I.; Hoffman, Y.; Knebe, A.; Sorce, J.G.; Steinmetz, M.; Tempel, E. The Undiscovered Ultradiffuse Galaxies of the Local Group. *Astrophys. J. Lett.* **2023**, *946*, L37. [CrossRef]
15. Chilingarian, I.V.; Bergond, G. SDSS J150634.27+013331.6: The second compact elliptical galaxy in the NGC 5846 group. *Mon. Not. R. Astron. Soc. Lett.* **2010**, *405*, L11–L15. [CrossRef]
16. Price, J.; Phillipps, S.; Huxor, A.; Trentham, N.; Ferguson, H.C.; Marzke, R.O.; Hornschemeier, A.; Goudfrooij, P.; Hammer, D.; Tully, R.B.; et al. The HST/ACS Coma Cluster Survey–V. Compact stellar systems in the Coma Cluster. *Mon. Not. R. Astron. Soc.* **2009**, *397*, 1816–1835. [CrossRef]
17. Chilingarian, I.; Zolotukhin, I. Isolated compact elliptical galaxies: Stellar systems that ran away. *Science* **2015**, *348*, 418–421. [CrossRef] [PubMed]
18. Evstigneeva, E.A.; Gregg, M.D.; Drinkwater, M.J.; Hilker, M. Internal Properties of Ultracompact Dwarf Galaxies in the Virgo Cluster. *Astron. J.* **2007**, *133*, 1722–1740. [CrossRef]

19. Bekki, K.; Couch, W.J.; Drinkwater, M.J.; Shioya, Y. Galaxy threshing and the origin of ultra-compact dwarf galaxies in the Fornax cluster. *Mon. Not. R. Astron. Soc.* **2003**, *344*, 399–411. [CrossRef]

20. Norris, M.A.; Kannappan, S.J.; Forbes, D.A.; Romanowsky, A.J.; Brodie, J.P.; Faifer, F.R.; Huxor, A.; Maraston, C.; Moffett, A.J.; Penny, S.J.; et al. The AIMSS Project—I. Bridging the star cluster–galaxy divide. *Mon. Not. R. Astron. Soc.* **2014**, *443*, 1151–1172. [CrossRef]

21. Minniti, D.; Kissler-Patig, M.; Goudfrooij, P.; Meylan, G. Radial Velocities of Globular Clusters in the Giant Elliptical Galaxy NGC 1399. *Astron. J.* **1998**, *115*, 121–129. [CrossRef]

22. Hilker, M.; Infante, L.; Vieira, G.; Kissler-Patig, M.; Richtler, T. The central region of the Fornax cluster—II. Spectroscopy and radial velocities of member and background galaxies. *Astron. Astrophys. Suppl. Ser.* **1999**, *134*, 75–86. [CrossRef]

23. Drinkwater, M.J.; Jones, J.B.; Gregg, M.D.; Phillipps, S. Compact Stellar Systems in the Fornax Cluster: Super-massive Star Clusters or Extremely Compact Dwarf Galaxies? *Publ. Astron. Soc. Aust.* **2000**, *17*, 227–233. [CrossRef]

24. Phillipps, S.; Drinkwater, M.J.; Gregg, M.D.; Jones, J.B. Ultracompact Dwarf Galaxies in the Fornax Cluster. *Astrophys. J.* **2001**, *560*, 201–206. [CrossRef]

25. Mieske, S.; Hilker, M.; Infante, L. Ultra compact objects in the Fornax cluster of galaxies: Globular clusters or dwarf galaxies? *Astron. Astrophys.* **2002**, *383*, 823–837. [CrossRef]

26. Drinkwater, M.J.; Gregg, M.D.; Hilker, M.; Bekki, K.; Couch, W.J.; Ferguson, H.C.; Jones, J.B.; Phillipps, S. A class of compact dwarf galaxies from disruptive processes in galaxy clusters. *Nature* **2003**, *423*, 519–521. [CrossRef]

27. Zapata, F.U.; Fellhauer, M.; Jara, A.A.G.; Carrillo, D.R.M.; Aravena, C.A. The formation of compact dwarf ellipticals through merging star clusters. *Mon. Not. R. Astron. Soc.* **2019**, *489*, 2746–2754. [CrossRef]

28. Brüns, R.C.; Kroupa, P.A. A catalog of extended clusters and ultra-compact dwarf galaxies—An analysis of their parameters in early- and late-type galaxies. *Astron. Astrophys.* **2012**, *547*, A65. [CrossRef]

29. Zhang, Y.; Bell, E.F. M32 Analogs? A Population of Massive Ultra-compact Dwarf and Compact Elliptical Galaxies in Intermediate-redshift Clusters. *Astrophys. J. Lett.* **2017**, *835*, L2. [CrossRef]

30. Mieske, S.; Hilker, M.; Jordán, A.; Infante, L.; Kissler-Patig, M.; Rejkuba, M.; Richtler, T.; Côté, P.; Baumgardt, H.; West, M.J.; et al. The nature of UCDs: Internal dynamics from an expanded sample and homogeneous database. *Astron. Astrophys.* **2008**, *487*, 921–935. [CrossRef]

31. Paudel, S.; Duc, P.-A.; Lim, S.; Poulain, M.; Marleau, F.R.; Müller, O.; Sánchez-Janssen, R.; Habas, R.; Durrell, P.R.; Heesters, N.; et al. The creation of a massive UCD by tidal threshing from NGC 936. *Mon. Not. R. Astron. Soc. Lett.* **2023**, *526*, L136–L142. [CrossRef]

32. Penny, S.J.; Forbes, D.A.; Strader, J.; Usher, C.; Brodie, J.P.; Romanowsky, A.J. Ultracompact dwarfs in the Perseus Cluster: UCD formation via tidal stripping. *Mon. Not. R. Astron. Soc.* **2014**, *439*, 3808–3816. [CrossRef]

33. Chilingarian, I.V.; Mieske, S.; Hilker, M.; Infante, L. Dynamical versus stellar masses of ultracompact dwarf galaxies in the Fornax cluster. *Mon. Not. R. Astron. Soc.* **2011**, *412*, 1627–1638. [CrossRef]

34. Karachentsev, I.D.; Karachentseva, V.E.; Huchtmeier, W.K.; Makarov, D.I. A Catalog of Neighboring Galaxies. *Astron. J.* **2004**, *127*, 2031–2068. [CrossRef]

35. Schweizer, F.; Seitzer, P.; Whitmore, B.C.; Kelson, D.D.; Villanueva, E.V. The Second Nucleus of NGC 7727: Direct Evidence for the Formation and Evolution of an Ultracompact Dwarf Galaxy. *Astrophys. J.* **2018**, *853*, 26. [CrossRef]

36. Chilingarian, I.V.; Cayatte, V.; Bergond, G. Stellar population constraints on the dark matter content and origin of ultra-compact dwarf galaxies. *Mon. Not. R. Astron. Soc.* **2008**, *390*, 906–912. [CrossRef]

37. Mayes, R.J.; Drinkwater, M.J.; Pfeffer, J.; Baumgardt, H.; Liu, C.; Ferrarese, L.; Côté, P.; Peng, E.W. Testing the tidal stripping scenario of ultracompact dwarf galaxy formation by using internal properties. *Mon. Not. R. Astron. Soc.* **2021**, *506*, 2459–2470. [CrossRef]

38. Fellhauer, M.; Kroupa, P. A possible formation scenario for the ultramassive cluster W3 in NGC 7252. *Mon. Not. R. Astron. Soc.* **2005**, *359*, 223–227. [CrossRef]

39. Kissler-Patig, M.; Jordán, A.; Bastian, N. The transition between star clusters and dwarf galaxies. *Astron. Astrophys.* **2006**, *448*, 1031–1035. [CrossRef]

40. Goodman, M.; Bekki, K. Formation of ultra-compact dwarf galaxies from supergiant molecular clouds. *Mon. Not. R. Astron. Soc.* **2018**, *478*, 3564–3575. [CrossRef]

41. Bekki, K.; Forbes, D.A.; Beasley, M.A.; Couch, W.J. Globular cluster formation from gravitational tidal effects of merging and interacting galaxies. *Mon. Not. R. Astron. Soc.* **2002**, *335*, 1176–1192. [CrossRef]

42. Chilingarian, I.V.; Mamon, G.A. SDSS J124155.33+114003.7—A missing link between compact elliptical and ultracompact dwarf galaxies. *Mon. Not. R. Astron. Soc. Lett.* **2008**, *385*, L83–L87. [CrossRef]

43. Makarova, L.N.; Tully, R.B.; Anand, G.S.; Lambert, T.S.; Sharina, M.E.; Koribalski, B.S.; Kraan-Korteweg, R.C. A Nearby Isolated Dwarf: Star Formation and Structure of ESO 006–001. *Astrophys. J.* **2023**, *943*, 139. [CrossRef]

44. Ferré-Mateu, A.; Durré, M.; Forbes, D.A.; Romanowsky, A.J.; Alabi, A.; Brodie, J.P.; McDermid, R.M. Low-mass compact elliptical galaxies: Spatially resolved stellar populations and kinematics with the Keck Cosmic Web Imager. *Mon. Not. R. Astron. Soc.* **2021**, *503*, 5455–5472. [CrossRef]

45. Ferré-Mateu, A.; Mezcua, M.; Barrows, R.S. A search for active galactic nuclei in low-mass compact galaxies. *Mon. Not. R. Astron. Soc.* **2021**, *506*, 4702–4714. [CrossRef]

46. Seth, A.C.; van den Bosch, R.; Mieske, S.; Baumgardt, H.; Brok, M.D.; Strader, J.; Neumayer, N.; Chilingarian, I.; Hilker, M.; McDermid, R.; et al. A supermassive black hole in an ultra-compact dwarf galaxy. *Natrue* **2014**, *513*, 398–400. [CrossRef]

47. Ahn, C.P.; Seth, A.C.; den Brok, M.; Strader, J.; Baumgardt, H.; van den Bosch, R.; Chilingarian, I.; Frank, M.; Hilker, M.; McDermid, R.; et al. Detection of Supermassive Black Holes in Two Virgo Ultracompact Dwarf Galaxies. *Astrophys. J.* **2017**, *839*, 72. [CrossRef]

48. Pechetti, R.; Seth, A.; Cappellari, M.; McDermid, R.; den Brok, M.; Mieske, S.; Strader, J. Detection of Enhanced Central Mass-to-light Ratios in Low-mass Early-type Galaxies: Evidence for Black Holes? *Astrophys. J.* **2017**, *850*, 15. [CrossRef]

49. Afanasiev, A.V.; Chilingarian, I.V.; Mieske, S.; Voggel, K.T.; Picotti, A.; Hilker, M.; Seth, A.; Neumayer, N.; Frank, M.; Romanowsky, A.J.; et al. A 3.5 million Solar masses black hole in the centre of the ultracompact dwarf galaxy fornax UCD3. *Mon. Not. R. Astron. Soc.* **2018**, *477*, 4856–4865. [CrossRef]

50. Ahn, C.P.; Seth, A.C.; Cappellari, M.; Krajnović, D.; Strader, J.; Voggel, K.T.; Walsh, J.L.; Bahramian, A.; Baumgardt, H.; Brodie, J.; et al. The Black Hole in the Most Massive Ultracompact Dwarf Galaxy M59-UCD3. *Astrophys. J.* **2018**, *858*, 102. [CrossRef]

51. Voggel, K.T.; Seth, A.C.; Baumgardt, H.; Mieske, S.; Pfeffer, J.; Rasskazov, A. The Impact of Stripped Nuclei on the Supermassive Black Hole Number Density in the Local Universe. *Astrophys. J.* **2019**, *871*, 159. [CrossRef]

52. Mayes, R.; Drinkwater, M.; Pfeffer, J.; Baumgardt, H. Supermassive black holes in UCDs formed from the nuclei of disrupted galaxies. *arXiv* **2023**, arXiv:2302.08082. [CrossRef].

53. Vasiliev, E. The Effect of the LMC on the Milky Way System. *Galaxies* **2023**, *11*, 59. [CrossRef]

54. Grion Filho, D.; Johnston, K.V.; Poggio, E.; Laporte, C.F.P.; Drimmel, R.; D'Onghia, E. A holistic review of a galactic interaction. *Mon. Not. R. Astron. Soc.* **2021**, *507*, 2825–2842. [CrossRef]

55. Tanaka, M.; Koike, M.; Naito, S.; Shibata, J.; Usuda-Sato, K.; Yamaoka, H.; Ando, M.; Ito, K.; Kobayashi, U.; Kofuji, Y.; et al. Galaxy Cruise: Deep Insights into Interacting Galaxies in the Local Universe. *Publ. Astron. Soc. Jpn.* **2023**, *75*, 986–1010. [CrossRef]

56. O'Ryan, D.; Merín, B.; Simmons, B.D.; Vojteková, A.; Anku, A.; Walmsley, M.; Garland, I.L.; Géron, T.; Keel, W.; Kruk, S.; et al. Harnessing the Hubble Space Telescope Archives: A Catalog of 21,926 Interacting Galaxies. *Astrophys. J.* **2023**, *948*, 40. [CrossRef]

57. Proshina, I.S.; Moiseev, A.V.; Sil'chenko, O.K. Young Star-Forming Complexes in the Ring of the S0 Galaxy NGC 4324. *Astron. Lett.* **2022**, *48*, 139–152. [CrossRef]

58. Martínez-Delgado, D.; Cooper, A.P.; Román, J.; Pillepich, A.; Erkal, D.; Pearson, S.; Moustakas, J.; Laporte, C.F.P.; Laine, S.; Akhlaghi, M.; et al. Hidden depths in the local Universe: The Stellar Stream Legacy Survey. *Astron. Astrophys.* **2023**, *671*, A141. . [CrossRef]

59. Nibauer, J.; Bonaca, A.; Johnston, K.V. Constraining the Gravitational Potential from the Projected Morphology of Extragalactic Tidal Streams. *Astrophys. J.* **2023**, *954*, 195. [CrossRef]

60. Tkachenko, R.; Korchagin, V.; Jmailova, A.; Carraro, G.; Jmailov, B. The Influence of the Galactic Bar on the Dynamics of Globular Clusters. *Galaxies* **2023**, *11*, 26. [CrossRef]

61. Block, D.L.; Bournaud, F.; Combes, F.; Groess, R.; Barmby, P.; Ashby, M.L.N.; Fazio, G.G.; Pahre, M.A.; Willner, S.P. An almost head-on collision as the origin of two off-centre rings in the Andromeda galaxy. *Nature* **2006**, *443*, 832–834. [CrossRef] [PubMed]

62. Katkov, I.Y.; Kniazev, A.Y.; Sil'chenko, O.K.; Gasymov, D. Star formation in outer rings of S0 galaxies—IV. NGC 254: A double-ringed S0 with gas counter-rotation. *Astron. Astrophys.* **2022**, *658*, A154. [CrossRef]

63. Zasov, A.V.; Saburova, A.S.; Khoperskov, A.V.; Khoperskov, S.A. Dark matter in galaxies. *Physics-Uspekhi (Adv. Phys. Sci.)* **2017**, *60*, 3–39. [CrossRef]

64. Boselli, A.; Fossati, M.; Longobardi, A.; Kianfar, K.; Dametto, N.Z.; Amram, P.; Anderson, J.P.; Andreani, P.; Boissier, S.; Boquien, M.; et al. A Virgo Environmental Survey Tracing Ionised Gas Emission (VESTIGE)—XII. Ionised gas emission in the inner regions of lenticular galaxies. *Astron. Astrophys.* **2022**, *659*, A46. [CrossRef]

65. Schweizer, F.; Seitzer, P. Remnant of a "Wet" Merger: NGC 34 and Its Young Massive Clusters, Young Stellar Disk, and Strong Gaseous Outflow. *Astron. J.* **2007**, *133*, 2132–2155. [CrossRef]

66. Bastian, N.; Schweizer, F.; Goudfrooij, P.; Larsen, S.S.; Kissler-Patig, M. Luminosity profiles and sizes of massive star clusters in NGC 7252. *Mon. Not. R. Astron. Soc.* **2013**, *431*, 1252–1263. [CrossRef]

67. Albareti, F.D.; Allende Prieto, C.; Almeida, A.; Anders, F.; Anderson, S.; Andrews, B.H.; Aragón-Salamanca, A.; Argudo-Fernández, M.; Armengaud, E.; Aubourg, E.; et al. The 13th Data Release of the Sloan Digital Sky Survey: First Spectroscopic Data from the SDSS-IV Survey Mapping Nearby Galaxies at Apache Point Observatory. *Astrophys. J. Suppl. Ser.* **2017**, *233*, 25. [CrossRef]

68. Collaboration, G.; Prusti, T.; de Bruijne, J.H.J.; Brown, A.G.A.; Vallenari, A.; Babusiaux, C.; Bailer-Jones, C.A.L.; Bastian, U.; Biermann, M.; Evans, D.W.; et al. The Gaia mission. *Astron. Astrophys.* **2016**, *595*, A1. [CrossRef]

69. Vallenari, A.; Brown, A.G.A.; Prusti, T.; de Bruijne, J.H.J.; Arenou, F.; Babusiaux, C.; Biermann, M.; Creevey, O.L.; Ducourant, C.e.a. Gaia Data Release 3. *Astron. Astrophys.* **2023**, *674*, A1. [CrossRef]

70. Yanny, B.; Rockosi, C.; Newberg, H.J.; Knapp, G.R.; Adelman-McCarthy, J.K.; Alcorn, B.; Allam, S.; Allende Prieto, C.; An, D.; Anderson, K.S.J.; et al. SEGUE: A Spectroscopic Survey of 240,000 Stars with g = 14–20. *Astron. J.* **2009**, *137*, 4377–4399. [CrossRef]

71. Majewski, S.R.; Schiavon, R.P.; Frinchaboy, P.M.; Allende Prieto, C.; Barkhouser, R.; Bizyaev, D.; Blank, B.; Brunner, S.; Burton, A.; Carrera, R.; et al. The Apache Point Observatory Galactic Evolution Experiment (APOGEE). *Astron. J.* **2017**, *154*, 94. [CrossRef]
72. Imig, J.; Price, C.; Holtzman, J.A.; Stone-Martinez, A.; Majewski, S.R.; Weinberg, D.H.; Johnson, J.A.; Prieto, C.A.; Beaton, R.L.; Beers, T.C.; et al. A Tale of Two Disks: Mapping the Milky Way with the Final Data Release of APOGEE. *Astrophys. J.* **2023**, *954*, 30. [CrossRef]
73. Belokurov, V.; Erkal, D.; Evans, N.W.; Koposov, S.E.; Deason, A.J. Co-formation of the disc and the stellar halo. *Mon. Not. R. Astron. Soc.* **2018**, *478*, 611–619. [CrossRef]
74. Haywood, M.; Di Matteo, P.; Lehnert, M.D.; Snaith, O.; Khoperskov, S.; Gómez, A. In Disguise or Out of Reach: First Clues about In Situ and Accreted Stars in the Stellar Halo of the Milky Way from Gaia DR2. *Astrophys. J.* **2018**, *863*, 113. [CrossRef]
75. Evans, T.A.; Fattahi, A.; Deason, A.J.; Frenk, C.S. How unusual is the Milky Way's assembly history? *Mon. Not. R. Astron. Soc.* **2020**, *497*, 4311–4321. [CrossRef]
76. Iorio, G.; Belokurov, V. The shape of the Galactic halo with Gaia DR2 RR Lyrae. Anatomy of an ancient major merger. *Mon. Not. R. Astron. Soc.* **2018**, *482*, 3868–3879. [CrossRef]
77. Helmi, A.; Babusiaux, C.; Koppelman, H.H.; Massari, D.; Veljanoski, J.; Brown, A.G.A. The merger that led to the formation of the Milky Way's inner stellar halo and thick disk. *Nature* **2018**, *563*, 85–88. [CrossRef] [PubMed]
78. Lane, J.M.M.; Bovy, J.; Mackereth, J.T. The stellar mass of the Gaia-Sausage/Enceladus accretion remnant. *Mon. Not. R. Astron. Soc.* **2023**, *526*, 1209–1234. [CrossRef]
79. García-Bethencourt, G.; Brook, C.B.; Grand, R.J.J.; Kawata, D. A high fidelity Milky Way simulation with Kraken, Gaia-Enceladus, and Sequoia analogues: Clues to their accretion histories. *Mon. Not. R. Astron. Soc.* **2023**, *526*, 1190–1197. [CrossRef]
80. Belokurov, V.; Kravtsov, A. From dawn till disc: Milky Way's turbulent youth revealed by the APOGEE+Gaia data. *Mon. Not. R. Astron. Soc.* **2022**, *514*, 689–714. [CrossRef]
81. Khoperskov, S.; Minchev, I.; Libeskind, N.; Haywood, M.; Di Matteo, P.; Belokurov, V.; Steinmetz, M.; Gomez, F.A.; Grand, R.J.J.; Hoffman, Y.; et al. The stellar halo in Local Group Hestia simulations—II. The accreted component. *Astron. Astrophys.* **2023**, *677*, A90. [CrossRef]
82. Rey, M.P.; Agertz, O.; Starkenburg, T.K.; Renaud, F.; Joshi, G.D.; Pontzen, A.; Martin, N.F.; Feuillet, D.K.; Read, J.I. VINTERGATAN-GM: The cosmological imprints of early mergers on Milky-Way-mass galaxies. *Mon. Not. R. Astron. Soc.* **2023**, *521*, 995–1012. [CrossRef]
83. Amarante, J.A.S.; Debattista, V.P.; Beraldo E. Silva, L.; Laporte, C.F.P.; Deg, N. Gastro Library. I. The Simulated Chemodynamical Properties of Several Gaia—Sausage—Enceladus-like Stellar Halos. *Astrophys. J.* **2022**, *937*, 12. [CrossRef]
84. Dillamore, A.M.; Belokurov, V.; Evans, N.W.; Davies, E.Y. Stellar halo substructure generated by bar resonances. *Mon. Not. R. Astron. Soc.* **2023**, *524*, 3596–3608. [CrossRef]
85. Davies, E.Y.; Dillamore, A.M.; Belokurov, V.; Evans, N.W. Stellar halo striations from assumptions of axisymmetry. *Mon. Not. R. Astron. Soc.* **2023**, *524*, 3821–3833. [CrossRef]
86. Belokurov, V.; Vasiliev, E.; Deason, A.J.; Koposov, S.E.; Fattahi, A.; Dillamore, A.M.; Davies, E.Y.; Grand, R.J.J. Energy wrinkles and phase-space folds of the last major merger. *Mon. Not. R. Astron. Soc.* **2023**, *518*, 6200–6215. [CrossRef]
87. Khoperskov, S.; Minchev, I.; Libeskind, N.; Belokurov, V.; Steinmetz, M.; Gomez, F.A.; Grand, R.J.J.; Hoffman, Y.; Knebe, A.; Sorce, J.G.; et al. The stellar halo in Local Group Hestia simulations—III. Chemical abundance relations for accreted and in situ stars. *Astron. Astrophys.* **2023**, *677*, A91. [CrossRef]
88. Naidu, R.P.; Conroy, C.; Bonaca, A.; Zaritsky, D.; Weinberger, R.; Ting, Y.S.; Caldwell, N.; Tacchella, S.; Han, J.J.; Speagle, J.S.; et al. Reconstructing the Last Major Merger of the Milky Way with the H3 Survey. *Astrophys. J.* **2021**, *923*, 92. [CrossRef]
89. Limberg, G.; Souza, S.O.; Pérez-Villegas, A.; Rossi, S.; Perottoni, H.D.; Santucci, R.M. Reconstructing the Disrupted Dwarf Galaxy Gaia-Sausage/Enceladus Using Its Stars and Globular Clusters. *Astrophys. J.* **2022**, *935*, 109. [CrossRef]
90. Vincenzo, F.; Spitoni, E.; Calura, F.; Matteucci, F.; Silva Aguirre, V.; Miglio, A.; Cescutti, G. The Fall of a Giant. Chemical evolution of Enceladus, alias the Gaia Sausage. *Mon. Not. R. Astron. Soc. Lett.* **2019**, *487*, L47–L52. [CrossRef]
91. Feuillet, D.K.; Feltzing, S.; Sahlholdt, C.L.; Casagrande, L. The SkyMapper-Gaia RVS view of the Gaia-Enceladus-Sausage—An investigation of the metallicity and mass of the Milky Way's last major merger. *Mon. Not. R. Astron. Soc.* **2020**, *497*, 109–124. [CrossRef]
92. Myeong, G.C.; Vasiliev, E.; Iorio, G.; Evans, N.W.; Belokurov, V. Evidence for two early accretion events that built the Milky Way stellar halo. *Mon. Not. R. Astron. Soc.* **2019**, *488*, 1235–1247. [CrossRef]
93. Khrapov, S.; Khoperskov, A.; Korchagin, V. Modeling of Spiral Structure in a Multi-Component Milky Way-Like Galaxy. *Galaxies* **2021**, *9*, 29. [CrossRef]
94. Titov, A.V.; Khoperskov, A.V. Numerical Modeling of the Collisions of Spheroidal Galaxies: Mass Loss Efficiency by Baryon Components. *Vestn. St. Petersburg Univ. Math.* **2022**, *55*, 124–134. [CrossRef]
95. Khrapov, S.S.; Khoperskov, A.V.; Korchagin, V.I. Numerical Modelling of the Dynamics of the Galactic Halos in the Colliding Galaxies. *Bull. South Ural. State Univ.-Ser.-Math. Model. Program. Comput. Softw.* **2019**, *12*, 123–135. [CrossRef]
96. Khoperskov, S.; Zinchenko, I.; Avramov, B.; Khrapov, S.; Berczik, P.; Saburova, A.; Ishchenko, M.; Khoperskov, A.; Pulsoni, C.; Venichenko, Y.; et al. Extreme kinematic misalignment in IllustrisTNG galaxies: The origin, structure, and internal dynamics of galaxies with a large-scale counterrotation. *Mon. Not. R. Astron. Soc.* **2021**, *500*, 3870–3888. [CrossRef]

97. Khrapov, S.; Khoperskov, A. Smoothed-particle hydrodynamics models: Implementation features on GPUs. *Commun. Comput. Inf. Sci.* **2017**, *793*, 266–277. [CrossRef]

98. Khoperskov, S.A.; Vasiliev, E.O.; Sobolev, A.M.; Khoperskov, A.V. The simulation of molecular clouds formation in the Milky Way. *Mon. Not. R. Astron. Soc.* **2013**, *428*, 2311–2320. [CrossRef]

99. Khoperskov, S.; Haywood, M.; Snaith, O.; Di Matteo, P.; Lehnert, M.; Vasiliev, E.; Naroenkov, S.; Berczik, P. Bimodality of [α Fe]–[Fe/H] distributions is a natural outcome of dissipative collapse and disc growth in Milky Way-type galaxies. *Mon. Not. R. Astron. Soc.* **2021**, *501*, 5176–5196. [CrossRef]

100. Monaghan, J.J.; Lattanzio, J.C. A Simulation of the Collapse and Fragmentation of Cooling Molecular Clouds. *Astrophys. J.* **1991**, *375*, 177–189. [CrossRef]

101. Vasiliev, E.O. Non-equilibrium ionization states and cooling rates of photoionized enriched gas. *Mon. Not. R. Astron. Soc.* **2011**, *414*, 3145–3157. [CrossRef]

102. Crain, R.A.; van de Voort, F. Hydrodynamical Simulations of the Galaxy Population: Enduring Successes and Outstanding Challenges. *Annu. Rev. Astron. Astrophys.* **2023**, *61*, 473–515. [CrossRef]

103. Deason, A.J.; Belokurov, V.; Koposov, S.E.; Lancaster, L. Apocenter Pile-up: Origin of the Stellar Halo Density Break. *Astrophys. J. Lett.* **2018**, *862*, L1. [CrossRef]

104. Grand, R.J.J.; Kawata, D.; Belokurov, V.; Deason, A.J.; Fattahi, A.; Fragkoudi, F.; Gimez, F.A.; Marinacci, F.; Pakmor, R. The dual origin of the Galactic thick disc and halo from the gas-rich Gaia-Enceladus Sausage merger. *Mon. Not. R. Astron. Soc.* **2020**, *497*, 1603–1618. [CrossRef]

105. Koppelman, H.; Helmi, A.; Veljanoski, J. One Large Blob and Many Streams Frosting the nearby Stellar Halo in Gaia DR2. *Astrophys. J. Lett.* **2018**, *860*, L11. [CrossRef]

106. Myeong, G.C.; Evans, N.W.; Belokurov, V.; Sanders, J.L.; Koposov, S.E. The Sausage Globular Clusters. *Astrophys. J. Lett.* **2018**, *863*, L28. [CrossRef]

107. Kruijssen, J.M.D.; Pfeffer, J.L.; Reina-Campos, M.; Crain, R.A.; Bastian, N. The formation and assembly history of the Milky Way revealed by its globular cluster population. *Mon. Not. R. Astron. Soc.* **2019**, *486*, 3180–3202. [CrossRef]

108. Torrealba, G.; Belokurov, V.; Koposov, S.E.; Li, T.S.; Walker, M.G.; Sanders, J.L.; Geringer-Sameth, A.; Zucker, D.B.; Kuehn, K.; Evans, N.W.; et al. The hidden giant: Discovery of an enormous Galactic dwarf satellite in Gaia DR2. *Mon. Not. R. Astron. Soc.* **2019**, *488*, 2743–2766. [CrossRef]

109. Boecker, A.; Neumayer, N.; Pillepich, A.; Frankel, N.; Ramesh, R.; Leaman, R.; Hernquist, L. The origin of stars in the inner 500 parsecs in TNG50 galaxies. *Mon. Not. R. Astron. Soc.* **2023**, *519*, 5202–5235. [CrossRef]

110. Hoyer, N.; Neumayer, N.; Seth, A.C.; Georgiev, I.Y.; Greene, J.E. Photometric and structural parameters of newly discovered nuclear star clusters in Local Volume galaxies. *Mon. Not. R. Astron. Soc.* **2023**, *520*, 4664–4682. [CrossRef]

111. Khoperskov, A.V.; Khoperskov, S.A.; Zasov, A.V.; Bizyaev, D.V.; Khrapov, S.S. Interaction between collisionless galactic discs and non-axisymmetric dark matter haloes. *Mon. Not. R. Astron. Soc.* **2013**, *431*, 1230–1239. [CrossRef]

112. Butenko, M.A.; Belikova, I.V.; Kuzmin, N.M.; Khokhlova, S.S.; Ivanchenko, G.S.; Ten, A.V.; Kudina, I.G. Numerical simulation of the galaxies outer spiral structure: The influence of the dark halo non-axisymmetry on the gaseous disk shape. *Math. Phys. Comput. Simul.* **2022**, *25*, 73–83. [CrossRef]

113. Navarro, J.F.; Frenk, C.S.; White, S.D.M. The Structure of Cold Dark Matter Halos. *Astrophys. J.* **1996**, *462*, 563–575. [CrossRef]

114. Zasov, A.V.; Khoperskov, A.V.; Zaitseva, N.A.; Khrapov, S.S. On the Formation of Spiral Arms in Dwarf Galaxies. *Astron. Rep.* **2021**, *65*, 1215–1232. [CrossRef]

115. Anders, F.; Khalatyan, A.; Chiappini, C.; Queiroz, A.B.; Santiago, B.X.; Jordi, C.; Girardi, L.; Brown, A.G.A.; Matijevic, G.; Monari, G.; et al. Photo-astrometric distances, extinctions, and astrophysical parameters for Gaia DR2 stars brighter than G = 18. *Astron. Astrophys.* **2019**, *628*, A94. [CrossRef]

116. Ge, X.; Gu, Q.S.; García-Benito, R.; Lu, S.Y.; Lei, C.L.; Ding, N. Observations of cold gas and star formation in dwarf S0 galaxies. *Mon. Not. R. Astron. Soc.* **2021**, *507*, 4262–4273. [CrossRef]

117. Vieira, K.; Korchagin, V.; Carraro, G.; Lutsenko, A. Vertical Structure of the Milky Way Disk with Gaia DR3. *Galaxies* **2023**, *11*, 77. [CrossRef]

118. Belokurov, V.; Zucker, D.B.; Evans, N.W.; Gilmore, G.; Vidrih, S.; Bramich, D.M.; Newberg, H.J.; Wyse, R.F.G.; Irwin, M.J.; Fellhauer, M.; et al. The Field of Streams: Sagittarius and Its Siblings. *Astrophys. J.* **2006**, *642*, L137–L140. [CrossRef]

119. Cunningham, E.C.; Sanderson, R.E.; Johnston, K.V.; Panithanpaisal, N.; Ness, M.K.; Wetzel, A.; Loebman, S.R.; Escala, I.; Horta, D.; Faucher-Giguère, C.A. Reading the CARDs: The Imprint of Accretion History in the Chemical Abundances of the Milky Way's Stellar Halo. *Astrophys. J.* **2022**, *934*, 172. [CrossRef]

120. Bassino, L.P.; Muzzio, J.C.; Rabolli, M. Are Globular Clusters the Nuclei of Cannibalized Dwarf Galaxies? *Astrophys. J.* **1994**, *431*, 634–639. [CrossRef]

121. Akins, H.B.; Christensen, C.R.; Brooks, A.M.; Munshi, F.; Applebaum, E.; Engelhardt, A.; Chamberland, L. Quenching Timescales of Dwarf Satellites around Milky Way-mass Hosts. *Astrophys. J.* **2021**, *909*, 139. [CrossRef]

122. Ramatsoku, M.; Serra, P.; Poggianti, B.M.; Moretti, A.; Gullieuszik, M.; Bettoni, D.; Deb, T.; Fritz, J.; van Gorkom, J.H.; Jaffé, Y.L.; et al. GASP—XVII. H I imaging of the jellyfish galaxy JO206: Gas stripping and enhanced star formation. *Mon. Not. R. Astron. Soc.* **2019**, *487*, 4580–4591. [CrossRef]

123. Zasov, A.V.; Saburova, A.S.; Egorov, O.V.; Moiseev, A.V. NGC 90: A hidden jellyfish galaxy? *Mon. Not. R. Astron. Soc.* **2020**, *498*, 101–109. [CrossRef]